

ANALYSIS OF THE STRUCTURAL AND INFLOW DATA FROM THE LIST TURBINE

Herbert J. Sutherland
Sandia National Laboratories*
Albuquerque, NM 87185-0708

ABSTRACT

The Long-term Inflow and Structural Test (LIST) program is collecting long-term, continuous inflow and structural response data to characterize the spectrum of loads on wind turbines. A heavily instrumented Micon 65/13M turbine with Phoenix 8m blades is being used as the test turbine for the first measurement campaign of this program. This turbine is located in Bushland, TX, a test site that exposes the turbine to a wind regime representative of a Great Plains commercial site. The turbine and inflow are being characterized with 60 measurements: 34 to characterize the inflow, 19 to characterize structural response, and 7 to characterize the time-varying state of the turbine. In this paper, an analysis of the structural and inflow data is presented. Particular attention is paid to the determination of the various structural loads on the turbine, long-term fatigue spectra and the correlation of various inflow descriptors with fatigue loads. For the latter analysis, the inflow is described by various parameters, including the mean, standard deviation, skewness and kurtosis of the hub-height horizontal wind speed, turbulence intensity, turbulence length scales, Reynolds stresses, local friction velocity, Obukhov length and the gradient Richardson number. The fatigue load spectrum corresponding to these parameters is characterized as an equivalent fatigue load. A regression analysis is then used to determine which parameters are correlated to the fatigue loads. The results illustrate that the vertical component of the inflow is the most important of the secondary inflow parameters on fatigue loads. Long-term fatigue spectra illustrate that extrapolation of relatively short-term data to longer times is consistent for the data reported here.

INTRODUCTION

The Long-term Inflow and Structural Test (LIST) program [1,2,3] is collecting long-term, continuous inflow and structural response data for wind turbines. The program is designed to characterize the extreme loads on the turbine and to determine the influence of various atmospheric parameters on fatigue loads. Madsen, Pierce and Buhl [4] note that the extreme loads during normal operation in turbulent conditions may cause the maximum turbine response, even higher than the loads experienced while parked in hurricane force winds. The highest operating loads dominate the fatigue damage to critical components (such as the blades) disproportionately, even though their rate-of-

* Sandia is a multiprogram laboratory operated by Sandia Corporation, a Lockheed Martin company, for the U.S. Department of Energy under contract DE-AC04-94AL85000.

occurrence is relatively small. Sutherland and Butterfield [5] present the views of a panel of experts convened to discuss these “extreme events.” They conclude that the nature of the turbulence responsible for, and the dynamic structural response to, these high load events is not understood at this time. They further conclude that characterizing these extreme conditions will drive down the cost of wind turbine systems.

To characterize the spectrum of these low-occurrence events requires a long-term, time-synchronized database that provides a detailed characterization of both the structural response of the wind turbine and the inflow for at least one full wind season. Previous studies have examined the influence of various inflow parameters on structural response. However, most of these studies are typically too short (i.e., hours of data taken over several days) to find the extremes, or they have limited inflow data. One notable exception is the study of Glinou and Fragoulis [6]. In this detailed study, multiple turbines in complex mountain terrain are characterized with large arrays of inflow and structural measurements. Their work is serving as a guide for the LIST program.

This paper presents a detailed analysis of the structural and inflow data obtained by the initial LIST measurement campaign. Particular attention is paid to the determination of the various structural loads on the turbine, long-term fatigue spectra and the correlation of various inflow descriptors with fatigue loads. The analysis is based on inflow and structural measurements that span a total of 333 hours (1998 ten-minute records) with average hub-height wind speeds up to almost 19 m/s. The data set is first divided into wind speed bins. All records below the cut-in wind speed of 5 m/s are discarded, leaving a total of 1017 ten-minute data records between 5 and 19 m/s. These records are then divided into Wind Speed bin classes based on their mean wind speed. This manuscript uses various sets of the data to illustrate general and specific trends in the data.

THE LIST TURBINE

The turbine used in the initial experimental campaign is a Micon 65/13M turbine, see Fig. 1. References 1 and 7 provide a complete description of the turbine, its site, and the instruments used to monitor the turbine and its inflow.

THE SITE

The turbine is located on the USDA-ARS site in Bushland, TX, see Fig. 2. In this figure, the test or LIST turbine is labeled turbine B. This site is characteristic of a Great Plains site with essentially flat terrain. The altitude in the middle of the site (at the base of the LIST turbine) is 1.168 km (3,833 ft). The test site is surrounded by farmland, and it slopes down approximately 1 m (3 ft) to the SSE across the span of the turbine bases (i.e., 76.4 m). To the NNW of the turbines is a reservoir with an approximately 1.2 m (4 ft) berm.

The primary wind direction at the site is from 215° , approximately SW.[†] The wind rosette for this site shows a secondary peak for winds from approximately due North.

As shown in Fig. 2, there are two buildings on the site. The first is the main control building that is WNW of the LIST turbine. The second is a small instrumentation enclosure that is downwind of the turbines. Neither the tank nor the buildings obstruct the inflow to the turbines from the prevailing wind direction. For inflow from the secondary wind direction (North), the LIST turbine will have an essentially unobstructed inflow.

THE TURBINE

The turbine used in this experimental investigation is a modified Micon 65/13 turbine (designated the 65/13M turbine). This turbine is a fixed-pitch, 3-bladed up-wind turbine with a three-phase 480 V asynchronous generator rated at 115 kW. The generator operates at 1200 rpm while the blades turn at a fixed 55 rpm.[‡] At hub height, the turbine stands 23 m (75 ft) tall on a tubular, 3-piece steel tower that weighs approximately 64.5 kN (14,500 lbs). The nacelle weight is approximately 42.7 kN (9,600 lbs).

Blades

The LIST turbine is fitted with Phoenix 8-m blades that are based on Solar Energy Research Institute (SERI)[§] airfoils. These blades are 7.9 m (312 in) long, yielding a rotor diameter of 17.1 m (55.9 ft). The blades are equipped with tip brakes. The split line for these brakes is located at 6.5 m (256 in) from the blade flange. With the blade mounted, the blade flange is located 599 mm (23.6 in) from the centerline of the low-speed shaft. The blades are a fixed-pitch design. The pitch is set to 2.2° at the 75 percent span line, per the instructions of J. Tangler [8].

O’Gorman and Simmermacher [9] and Simmermacher, O’Gorman, Martin and Lopez [10] characterize the static and dynamic properties of the blades. The weight of the 3 blades varies between 3.31 and 3.34 kN (745 and 750 lbs). Their center of gravity is located approximately 2.36 m (93 in) from the blade flange. The chordwise moment-of-inertia, I_{zz} , was measured to be 1533 kg-m^2 ($5.25 \times 10^6 \text{ lb-in}^2$) ± 20 percent [9].

Modal Survey

Simmermacher, et al. [10] report the results of a modal survey of the blades in a ‘free-free’ configuration, i.e., the blades are suspended by nylon straps for the survey. All 31 modes found in the survey are complicated combined modes; namely, the modes are combinations of edge and flap motion. The first mode is primarily flap motion (probably

[†] All compass headings are given with-respect-to True North.

[‡] The turbine is a used machine that ran in the Palm Springs (CA) area for approximately 15 years. During that period, several turbine subsystems were modified to increase performance and reliability. These systems include the brakes, gearbox, generator and blades. The standard Micon 65/13 turbine rotates at a fixed 45 rpm.

[§] SERI is now the National Renewable Energy Laboratory (NREL).

the first bending mode of the blade). Its frequency is 8.21 Hz with a damping of 1.16 percent. The next mode, at 14.75 Hz with a damping of 1.70 percent, primarily consists of tip motion in the edgewise direction. The third mode, best described as the second flap-bending mode, occurs at 16.8 Hz with a damping of 1.06 percent. The mode best described as the first edgewise-bending mode occurs at 64.49 Hz with a damping of 1.02 percent.

Simmermacher and Carne [11] report the results of a modal survey of the tower. The modal survey of the tower, without the nacelle attached, yields a first bending mode of 3.29 Hz with 2.4 percent damping in the fore-aft direction (with respect to the prevailing wind direction of 215°) and 3.31 Hz with 2.6 percent damping in the side-to-side direction. The second bending modes are 15.27 and 15.76 Hz with 4.6 and 3.5 percent damping, respectively.

SISTER TURBINES

Two additional Micon 65/13M turbines are also located at the test site. These turbines are equipped with Aerostar 7.5 m (292 in) blades. The three turbines are sited in a straight line normal to the prevailing wind direction of 215°. The turbine centerlines are spaced at a distance of 2.25 diameters,** 38.2 m (125.3 ft) apart. The positions of the turbines are shown in Fig. 2. In this diagram, the turbines are labeled A, B and C. A and C turbines are the Aerostar-fitted turbines and Turbine B is the LIST turbine with the Phoenix blades.

These turbines are being used to provide reference data for a “standard” configuration of the turbine.

PREVIOUS TESTS

Tangler, et al. [12, 13, 14] reported on the test of a similar turbine located in San Geronio Pass, California. The data from that turbine is not directly comparable to the data cited here because the blades and the turbines are very different. In particular, the turbine tested here has a larger generator and a faster rotation rate (115 kW and 55 rpm vs. 65 kW and 45 rpm).

Although built by the same manufacturer, the blades tested here are also different. Namely, they reflect the difference between a prototype and production blade. First, they are approximately 0.45 kN (100 lb) heavier. The modal tests reported by Tangler, et al. [13, 14] were conducted with the blade fixed to the hub assembly. Their results for the first flap and edgewise-bending modes are 3.16 Hz and 7.2 Hz, respectively. The difference between the two sets of modal measurements can be attributed to the differences in the test conditions (‘fixed-free’ vs. ‘free-free’) and to the differences in the weight of the blades.

** Unless noted, dimensions given in diameters are referenced to the diameter of the Phoenix blade set.

INSTRUMENTATION AND DATA SYSTEM

The turbine and its inflow are monitored using 60 sensors: 34 to characterize the inflow, 19 to characterize structural response, and 7 to characterize the time-varying state of the turbine. Jones, et al. [7] provides a complete description of the instrumentation.

Inflow Instrumentation

The inflow into the LIST turbine is heavily monitored with sonic anemometers, cup anemometers and wind vanes. When the latter two are used in combination with one another, they are commonly called a cup-and-vane combination. A schematic diagram of the inflow instrumentation is shown in Fig. 3.

The inflow instrumentation is located approximately 30.7 m (101 ft), in front of the turbines (with respect to the prevailing wind). This dimension is equivalent to 2.0 diameters for the standard AeroStar blade set and 1.8 diameters for the Phoenix blade set.

As shown in Fig. 3, a cup-and-vane combination is used to monitor the horizontal inflow velocity and direction at hub height. Additional cup anemometers are used to measure horizontal inflow velocity at the top and bottom of the rotor disk and 1.6 m (5.1 ft) above ground level.

Five (5) sonic anemometers are used to obtain a more detailed description of the inflow. These anemometers are placed in a circular pattern as shown in Fig. 3. The diameter of the circle is the same as the diameter of the rotor disk. Each sonic anemometer measures three components of the inflow velocity (two horizontal and one vertical) and the sonic temperature. The quoted accuracy of these instruments is ± 0.02 m/sec on velocity and $\pm 0.01^\circ\text{C}$ on temperature. The units have a 200 Hz internal sample rate and a 12-bit internal representation. A digital-to-analogue interface is used to change this internal digital representation to an analogue signal compatible with the data acquisition system.

As noted, all of these instruments are aligned with the prevailing wind direction of 215° . For this site, a secondary wind direction is approximately True North. To obtain an accurate measurement of the inflow when winds are from this secondary direction, an auxiliary anemometer tower is set at 12° with-respect-to the LIST turbine at a distance of 1.84 diameters, 31.3 m (102.6 ft). This tower is instrumented with a cup-and-vane combination that is aligned with the rotor hub. When inflow is from this secondary direction, the sonic anemometers experience some blockage and will not provide an accurate description of the inflow.

The inflow into the other two turbines is monitored with hub-height cup-and-vane combinations, located 1.84 rotor diameters, 31.3 m (102.6 ft), upwind (215°) of each turbine.

In addition to these velocity measurements, the temperature, differential temperature and barometric pressure are also measured. The temperature is measured at 1.6 m (5.1 ft) above ground level. The differential temperature is measured between the top of the

rotor [33.6 m (110 ft)], and the ground level temperature (1.6 m). The barometric pressure is measured at 2.13 m (7 ft) above ground level, inside a breathable instrument enclosure.

Structural Instrumentation

The structural response of the turbine is measured with a variety of gauges, primarily strain gauges. A schematic of their placement is shown in Fig. 4. Each blade is instrumented with root and 40-percent-span gauge sets that measure flap and edgewise bending. The tower is instrumented with bending gauges located 3.9 m (154 in) above the turbine base. These gauge sets measure tower fore-and-aft and side-to-side bending (relatively to the prevailing wind direction). All strain gauges are calibrated using static loading.

The acceleration of the nacelle is monitored using two semiconductor strain-gage type accelerometers. These single-axis accelerometers are attached to the main frame of the nacelle. They are positioned to measure the horizontal acceleration parallel and perpendicular to the current yaw position of the turbine.

Additional Instrumentation

In addition to the instrumentation cited above, several other turbine parameters are measured. These include yaw position, rotor position, rotor speed, and control monitor (on-off switch). The yaw and rotor positions are measured directly with 360° angle encoders. The rotor speed is derived from the rotor position using a dedicated, differentiating analogue circuit. The power produced by each of the three turbines is also monitored.

DATA SYSTEM

The instruments cited above are monitored continuously using the Accurate, GPS Time-Linked Data Acquisition System, ATLAS, described in detail by Berg and Zayas [15]. The system monitors a total of 75 channels: 60 instrument channels and 15 time and status channels. The clocks on the system maintain a 1 micro-second accuracy using satellite links to the Global Positioning Satellite (GPS) system.

The 12-bit data stream is monitored at a rate of 30 Hz. This yields a Nyquist Frequency of 15 Hz, which is sufficient for capturing the behavior of the inflow and the structural response of the turbine. ATLAS uses a second-order anti-aliasing active filter followed by a programmable fifth-order Butterworth filter. The cut-off frequency for the latter filter was set to 15 Hz.

The data system automatically segments the data into ten-minute blocks, converts the data into engineering units, and archives them for future processing.

THE DATA SET

The distribution of the 1017 ten-minute records with mean wind speeds above 5 m/s is summarized in Fig. 5. As illustrated by this figure, the records are divided into wind speed classes for this analysis. Wind speed bin class 3 encompasses speeds to 9 m/s (the sum of the first two columns in Fig. 5). Bin classes 4, 5, 6 and 7 encompass speed ranges of 9-11, 11-13, 13-15 and 15-17 m/s, respectively. Bin class 8 encompasses all wind speeds above 17 m/s. As illustrated in this figure, 186 records are above 11 m/s mean wind speed. No ten-minute record has a mean wind speed above 19 m/s.

TYPICAL INFLOW DATA

A typical set of inflow data is shown in Figs. 6 through 11. The data in these illustrations are taken from a ten-minute record. For this record, the average wind speed is 12.2 m/s, the turbulence intensity is 11.9 percent, and its average direction is 225°.

Fig. 6 compares the horizontal wind speed at the hub-height as measured by a sonic and a cup anemometer that are co-located at hub height on the center anemometer tower, see Fig. 3. The direction of the horizontal component of the wind speed for a sonic and a vane anemometer are compared in Fig. 7. The measurements are in close agreement, with the data from the sonic anemometer illustrating its faster response time.

Fig. 8 illustrates the vertical velocity (positive up) at hub height as measured by a sonic anemometer on the center anemometer tower. For most of this rather turbulent period, the vertical wind speed is varying between ± 1 m/s; however, at approximately 16 seconds, the wind speed exceeds 2.5 m/s.

From the sonic wind speed data, the instantaneous Reynolds stress components can be determined, see the Appendices. The horizontal/vertical Reynolds stress, $u'w'$, is shown in Fig. 9. These instantaneous values led to an average local friction velocity u^* of 0.63 m/s for this ten-minute record. These inflow parameters are defined in the appendices.

In addition to hub-height data, measurements are also made across the rotor. The horizontal wind speed from the bottom to the top of the rotor is shown in Fig. 10. The wind speed across the rotor is shown in Fig. 11.

TYPICAL STRUCTURAL DATA

The structural response of the LIST turbine blades is monitored using 6 bending-gauge circuits on the hub and 6 at the 40 percent span of the blades. Both flap and edge moments are measured at each of these stations. A typical set of time-series data for edge and flap bending is shown in Figs. 12 and 13. The strain gauge data in these two figures correspond to the same ten-minute data set cited in Figs. 6 through 11.

TYPICAL POWER DATA

Typical power data are shown in Fig. 14 for Turbines B (the LIST turbine) and C. During this period, the LIST turbine is producing between 50 and 100 KW, while Turbine C is producing between 25 and 60 KW. This difference is directly attributable to the increase in the size, efficiency and speed of the SERI/Phoenix blades. These data correspond to the wind speed data shown in Fig. 6 through 11.

ANALYSIS TECHNIQUES

Various analysis techniques are used to analyze this data set. This section summarizes these techniques.

INFLOW ANALYSIS

Many parameters have been proposed to quantize the influence of the inflow on wind turbine loads. The mean wind speed and turbulence intensity are the most widely recognized as having the major influence on loads. Rohatgi and Nelson [16], Fragoulis [17], Glinou and Fragoulis [6] and Kelley, et al. [18, 19] discuss additional parameters. Sixteen (16) of these secondary parameters are determined from the data in each of the ten-minute data sets cited here.

Justifying the inclusion or exclusion of a parameter in this list and detailing its physical significance is beyond the scope of this paper. Rather, the purpose of this paper is to continue to quantify their influence on turbine fatigue loads. As the quantifying process continues, many of these parameters will be discarded and others may be added.

The symbols and underlying mathematical formulations for the various inflow and structural parameters are presented in the Appendices.

FATIGUE CYCLE COUNTING

For the analyses presented here, the fatigue spectra (range-only cycle counts) are determined by rainflow counting the time-series bending moment data using the CRUNCH [20] data analysis program. This analysis closes all cycles and counts half-cycles as full cycles. For the cycle counts presented here, the appropriate ten-minute records are concatenated, placed end-to-end, and counted as a single file [21].

The output of this analysis is a histogram (or probability density function) of the number and magnitude of the fatigue cycles. The histogram is divided into a finite number of cells that form the "cycle count matrix" for the fatigue spectrum. Each of the matrix's I cells, commonly called bins, contains the count, n_i , of the fatigue cycles that fall within the range of magnitudes prescribed for that cell. For this analysis, evenly spaced bins are used, and the characteristic bin load F_i is taken to be the midpoint of the magnitudes covered by the i^{th} bin [21].

EQUIVALENT FATIGUE LOAD

The equivalent fatigue load [21, 22] is used to quantize the fatigue damage contained in spectral load distributions contained in each ten-minute record. In general, the equivalent fatigue load is determined using Miner's Rule to combine the spectral components into a single, constant-rate fatigue load that will produce equivalent damage. For the case of a constant mean (range-only cycle counts) and a power law S-N curve with a fatigue exponent of m [21, 23], the equivalent cyclic load F_e has the form:

$$F_e = \left[\frac{\sum_{i=1}^I (F_i)^m n_i}{N_o} \right]^{1/m}, \quad [1]$$

where F_e is the equivalent fatigue load at a total of N_o fatigue cycles.

The choice of N_o is somewhat arbitrarily. It is sometimes chosen to be a number of cycles suitable for laboratory testing, i.e., 10^6 cycles [22]. Other times, it is chosen to be approximately the average number of cycles recorded in the data set; i.e., the average number of cycles in a ten-minute data set. If data are not available, then the choice of N_o may be based upon the rotational frequency f_o of the turbine [6, 21]. Since the choice of N_o is arbitrary and does not influence the comparative nature of the analysis presented here, we will assume a constant value for N_o of 2000 cycles for the equivalent-fatigue-load data analysis. This choice for N_o yields a value for F_e that is near the average mean of the range of the fatigue cycles.

As illustrated in Eq. 1, F_e is not unique for a given load spectra. Not only does it depend on the choice of N_o , but it also depends on the fatigue exponent m . For comparison purposes, F_e is usually reported for multiple values of m . Typical values for m are 3 for welded steel, 6 for extruded aluminum and 10 for fiberglass composite materials.

MULTI-VARIABLE FITTING ROUTINE

The multi-variable fitting routine used to fit the various inflow parameters to the equivalent fatigue load is based on the general linear least squares routine described by Press, Teukolsky, Vetterling and Flannery [24]. Their routine determines a generalized fit to a set of points (x_i, y_i) for the basis functions X_k by determining values for the parameters a_k which minimize the merit function χ^2 :

For a set of basis functions of the form:

$$\hat{y}(x) = \sum_{k=1}^M a_k X_k(x), \quad [2]$$

the merit function is:

$$\chi^2 = \sum_{i=1}^N \left[\frac{y_i - \hat{y}(x)}{\sigma_i} \right]^2, \quad [3]$$

where σ_i is the measurement error (standard deviation) of the i^{th} data point. If the measurement errors are not known, they may all be set to the constant value of one [24].

The basis functions are arbitrary fixed functions of x ; they are not necessarily polynomials. As pointed out by the authors of this algorithm: “if you are willing to tolerate a bit of programming hack,” the generalized fitting techniques they employ may be expanded from the dependence on a single variable x to a dependence on a vector variable \mathbf{x} , i.e., a set of variables x_k .

For the analysis presented here, the basis function for each variable that composes the vector $\mathbf{x} = (x_1, x_2, \dots, x_k, \dots, x_K)$ is assumed to be a polynomial of the form:

$$X_k(x_k) = \sum_{j=1}^P a_{kj} (x_k)^j, \quad [4]$$

and the measurement error σ_i is assumed to be one, see Eq. [3]. For these assumptions, Eq. 3 becomes:

$$\chi^2 = \sum_{i=1}^N \{y_i - \hat{y}(x)\}^2, \quad [5]$$

where

$$\hat{y}[x] = a_0 + \sum_{j=1}^P a_{kj} (x_k)^j. \quad [6]$$

In the Mounturb report [6], the value of P is taken to be 1, i.e., a linear fit. With this additional assumption, Eq. 6 becomes:

$$\hat{y}(x) = a_0 + a_1 x_1 + a_2 x_2 + \dots + a_M x_M. \quad [7]$$

The form shown in Eq. [7] is the one used in the analysis presented here.

DEPENDENCE COEFFICIENT

Quantifying the influence of each inflow parameter on fatigue loads requires the development of a “dependence coefficient.” The one proposed by Glinou and Fragoulis [6] is “the relative per sigma dependence coefficient S_k for each parameter.” For a linear formulation, as given in Eq. 7, S_k has the following form:

$$S_k = \frac{a_o + a_1 \bar{x}_1 + a_2 \bar{x}_2 + \dots + a_k [\bar{x}_k + \sigma(x_k)] + \dots + a_K \bar{x}_K}{a_o + a_1 \bar{x}_1 + a_2 \bar{x}_2 + \dots + a_K \bar{x}_K} - 1$$

$$= a_k \frac{\sigma(x_k)}{\bar{y}}$$
[8]

Thus, S_k measures the normalized effect of increasing the k^{th} parameter by one standard deviation, $\sigma(x_k)$, from its mean, \bar{x}_k , with the result normalized by the mean value, \bar{y} , of the dependent variable \hat{y} .

GUMBEL DISTRIBUTION

Estimating the extreme values of bending moments entails fitting a distribution to the extreme values. As discussed by Madsen et al. [25] and Laino et al. [26], the distribution of the maximum bending moment in each ten-minute record is assumed to follow a Gumbel distribution. This distribution, also called an Extreme Value Type 1 distribution has the following form:

$$F(x; \alpha_E, \beta_E) = \exp\{-\exp[-\alpha_E(x - \beta_E)]\}$$
[9]

where F is the cumulative density function of the variable x , and α_E and β_E are the scale and location parameters. For a set of data with n points, the values of α_E and β_E can be estimated using the following [25, 26]:

$$\alpha_E = \frac{\ln(2)}{2 \left(\frac{1}{n} \sum_{r=1}^n \frac{r-1}{n-1} x_r \right) - \bar{X}}$$
[10]

and

$$\beta_E = \bar{X} - \frac{\gamma_E}{\alpha_E}$$
[11]

where γ_E is Euler's constant (0.5772).

DATA ANALYSIS

TURBINE PERFORMANCE

Performance parameters for each turbine are shown in Figs. 15 and 16. In both plots, the wind speed increment is 0.5 m/s. The solid symbols present data from bins that contain a minimum of 5 hours of data. Open symbols present data from bins that have a minimum of 1 hour of data but less than 5 hours of data. The data is not corrected for the altitude of the site.

As shown by the “power curves” in Fig. 15, the Phoenix blades produce significantly more energy than the Aerostar blades, with the former producing a maximum of approximately 100 kW and the latter producing approximately 60 kW. Both reach rated capacity at approximately 15 m/s. The Phoenix blades start producing power at approximately 4.0 m/s and the Aerostar blades at approximately 5.5 m/s. At the Bushland site, these power curves translate to an estimated power production of 130 MWh from the LIST turbine and an average of 77.5 MWh from the other two turbines. Thus, the Phoenix blades nearly double the annual energy production of the Aerostar blades.

In the initial study of the power produced by similar turbines in San Geronio Pass, CA, the maximum power production is approximately 65 and 70 kW respectively, [14]. The Phoenix blades are not optimized for maximum power production due to the limited capacity of the gearbox and generator. Thus, the increase in rotor speed in the modified turbines significantly increases their power production from the Phoenix 8-m blades.

As these turbines have different diameters and speeds, the plot of their power coefficient shown in Fig. 16 is a better comparison of the performance. As illustrated by this plot, the Phoenix blades peak with a power coefficient of approximately 0.43 at the tip speed ratio of approximately 6.1. This tip speed ratio corresponds to an inflow velocity of approximately 8 m/s. For the Aerostar blades, the maximum power coefficient is approximately 0.32 at a tip speed ratio of 4.1 (approximately 9 m/s). Tangler et al. [12] reports a maximum power coefficient for the Phoenix blades of approximately 0.41.

STRUCTURAL RESPONSE

The extensive structural data for this turbine permits a detailed analysis of the structural response of the turbine. For this report, we will concentrate on the dynamics of the turbine’s blades.

Azimuth-Averaged Edge-Bending Moment

Average edge-bending moments, as a function of the azimuth position, are shown in Fig. 17. These illustrations are derived from the time series data shown in Figs. 6 through 13.

The blade weight, see O’Gorman and Simmermacher [9], varies between approximately 3.31 and 3.34 kN (745 and 750 lbs). Their centers of gravity are located at approximately 2.36 m (93 in) from the blade flange. Thus, the edge-bending moment at the root of the blade due to gravity should be approximately 8.8 kN-m when the blade is horizontal. When the mean is removed from the data shown in Fig. 17a, the variation in bending moments ranges between 8.5 kNm at an azimuth position of 90° and 8.4 kNm at 270°.

A similar plot for the edge-bending stress in the blade at the 40 percent span location is shown in Fig. 17b. In this figure, data for blades 2 and 3 are shown. These plots are essentially overlays of one another when Blade 2’s plot is shifted 120°.

Power Spectral Density

The power spectral densities (PSD) for root edge and flap bending for the Phoenix blades during normal operation are shown in Fig. 18. This figure illustrates that the Phoenix blades are very active at all multiples of the rotational speed. The primary harmonics, in both the edge and flap directions, occur at the system rotation rate, 1P, of 0.92 Hz (55 rpm). The other multiplies of the rotation rate are represented by spikes in the PSD curve.

Tangler et al. [14] reports significantly less response than the response measured here. The increased response measured here is to be expected because the Phoenix blades are optimized for a rotation speed of 45 rpm.

As shown in Fig. 18a, the edge-bending response of the blades has two major peaks at 1P (0.92 Hz) and 7P (6.42 Hz). In the earlier test series, major peaks are observed at 1P (0.75 Hz) and 9P (6.75 Hz). As the first edge mode of the blade/hub combination occurs at approximately 7 Hz [14], the large resonance observed in Fig. 6b at 7P and the corresponding resonance observed by Tangler et al. [14] at 9P is expected.

The flap bending response, see Fig. 18b, also illustrates the very active nature of this blade/turbine combination, with major peaks occurring at the first four multiplies of 1P. The data presented by Tangler et al. [14] yield similar results, except for the peak at 3P, which is not present in their locked-yaw data. With active yaw, the 3P harmonic dominates and the 4P is significantly reduced.

FATIGUE LOADS AND ANALYSIS

Long-Term Fatigue Load Spectrum

One of the objectives of the LIST program is to obtain long-term fatigue spectra for the turbine blade loads. The long-term fatigue spectra for 118 ten-minute records in wind class 5 offer an important database for studying long-term fatigue spectrum. These data are summarized in Figs. 19 and 20. Figure 19 presents the histogram of the cycle count data and Fig. 20 presents an exceedance plot of the data.

In these two figures, the fatigue spectra are typical for this class of turbines. Namely, the edge-bending spectra display a bi-modal distribution, see Figs. 19a and 20a, that is directly attributed to the large 1P gravity component of the bending moment, see Figs. 12 and 18a. As illustrated in Figs. 19b and 20b, the fatigue spectrum for flap-bending moment has a very different character, with a single-mode distribution.

In Fig. 19, the 20-hour data are contrasted to one-hour data. In Fig. 20, the 20-hour data are contrasted to one-hour and the seven-hour data. These comparisons illustrate the importance of long-term data sets. In particular, the one-hour data spectra have a so-called “floor” occurring at approximately 1 cycle count per hour. This floor is easily observed in the data presented in Fig. 19a and b in bins above approximately 30 kNm and 25 kNm, respectively. As the bins that constitute the floor of the data contain only a

single cycle count each, using them as an estimate of the long-term behavior would not be accurate because the number of observations is not statistically significant.

When more data are added (20 times more in this case), the floor is lowered to approximately 0.05 cycles per hour, i.e., one cycle in 20 hours. In both the edge and the flap bending cases, the seven-hour exceedance curve lies virtually on top of the one-hour curve until the floor in the one-hour data set is reached.

The significant difference between the various data sets is that the expansion of the data set to 20 hours extends the exceedance curve to a new floor. In particular, the additional data indicates that the primary slope of the exceedance curve in the high bending moment region of the spectrum continues unabated past the floor of the one-hour data set.

These data indicate that the extrapolation of relatively short-term spectra to long-term spectra is consistent with measured data. And, based on the data analyzed here, the high-stress tail of the distribution continues to at least a floor of 1 count in 20 hours, with indications that this pattern will continue.

Dependence on Inflow Parameters

As accepted throughout the wind industry, the primary inflow parameters that influence turbine fatigue damage are the mean wind speed and turbulence (turbulence intensity). Discussed above and outlined in the Appendices are a large number of secondary inflow parameters that may also influence fatigue loads. Of these proposed parameters, a total of 16 secondary parameters are examined; the influence of the two primary parameters is not examined here. Using the analyses described above, the linear, multi-variable fit, Eq. 7, is used to determine the relationships between the inflow parameters and the equivalent fatigue load, Eq. 1. Using the values for a_k derived by the fitting process, the dependence coefficient, Eq. 8, is determined for each of the 16 inflow variables. This process is repeated for flap and edge bending loads and for three values of the material exponent, m ; namely, 3, 6 and 10, which correspond to welded steel, aluminum and fiberglass, respectively. Results for the dependence of the equivalent fatigue load on the 16 inflow parameters are shown in Figs. 21 through 25.

Bin Class 5 Wind Speeds

Figure 21 presents the suite of dependency coefficients determined for bin class 5 wind speeds (11 to 13 m/s). The analysis is based on 118 ten-minute records.

As shown in Fig. 21a for flap bending loads, the Richardson number is the most important of the group of inflow variables examined here for flap bending. It is followed closely by the cross-velocity Reynolds stresses, $u'w'$ and $v'w'$, and the vertical shear exponent α . For edge bending, see Fig. 21b, the $v'w'$ Reynolds stress and the standard deviation of the vertical wind component σ_w (i.e., a measure of the vertical turbulence), are the most important, followed by the Richardson number and the cross-rotor, horizontal turbulence length scale, L_v . Note that the correlation of the edge fatigue loads to all of the inflow parameters is significantly less than that of the flap loads.

Other Wind Speed Bin Classes

Plots of the dependence coefficient for flap bending in other wind speed bin classes are shown in Figs. 22, 23, 24 and 25. These analyses are based upon 116, 24, 21 and 23 ten-minute records, respectively.

As shown in these figures, the dependency of the equivalent fatigue load varies widely across the wind speed bin classes. The general trend is less dependence on the Richardson number and more dependence on the various terms that are affected by the cross velocities v and, especially, w for increasing wind speed. In particular, the local friction velocity, u^* , becomes predominant at higher wind speeds.

Similar results have been found for edge bending.

Discussion

The vertical component of the inflow arises as the most-important characteristic of the inflow that influences fatigue loads. Similar results are reported by Fragoulis [17]. The atmospheric stability term, Richardson number, also plays an important role.

LOAD EXTREMES

The extreme loads are one of the major drivers in the design of wind turbines. The time-synchronized data provided by LIST provides a detailed look at these events.

Long-Term Ultimate Loads

Madsen, Pierce and Buhl [25] and Laino and Pierce [26] have addressed the statistical uncertainty of loads prediction using structural dynamics simulation codes. The data presented here offer measured data that may be used to examine load extremes for the operating wind turbine.

The extreme load in each ten-minute data set for bin class 5 wind speeds is shown in Fig. 26. For edge bending loads, the mean value is 18.55 kNm with a standard deviation of 1.52 kNm; i.e., a covariance (ratio of the standard deviation to the mean) of 8.21 percent. For flap, these values are 15.28 kNm, 2.47 kNm, and 16.17 percent, respectively. Following the lead of Refs. 25 and 26, the distribution of the measured, maximum bending-moment from each ten-minute record is fit with a Gumbel distribution, Eqs. 9 through 11. The fit for both edge and flap bending are shown in Fig. 27 (a Gumbel distribution will plot as a straight line for the axis system used in this figure). Similar plots are obtained for lower wind speed bins. For the higher wind speed bins, there are only approximately 20 records in each bin, see Fig. 5. Thus, these data are probably too sparse to warrant fits [26], although a Gumbel distribution fits the bin class 8 wind speed extremes very well, see Fig. 28.

The analytical data reported in Refs. 25 and 26 follow a Gumbel distribution very closely. While the measured data shown in Fig. 27 follow the body of a Gumbel distribution, they tend to diverge from it at both the high and low extremes. One factor that may account

for this difference is that the analytical study is based on the analysis of a stationary process with a constant mean wind speed. This is in sharp contrast to the measured data, which cover a range of mean wind speeds and is not stationary. Thus, the analytical data set is very closely controlled and one would expect that it would follow the Gumbel distribution.

Another possible factor is simply that there are not enough data to permit a precise determination of the distribution's extremes. For data at a single mean wind speed, Laino et al. [26] demonstrate that approximately 50 ten-minute data sets are sufficient for consistent results. As the wind speed bin width increases, this number may increase as well, although for bin class 8 wind speeds the fit appears to follow the Gumbel distribution very well, see Fig. 28. Moreover, in wind speeds bins that contain more ten-minute records, the divergence at the extremes is still observed.

And, finally, maybe there is the possibility that the process that produces the body of the distribution is different from the process that is producing the extreme of the distribution. A detailed examination of all of the inflow and operational parameters at each extreme event may be able to determine if indeed this is the case. Such a detailed examination of one of the largest extreme flap loads is discussed in the next section of this paper. For that extreme, there does not appear to be an extraordinary inflow event producing the load extreme. Rather, the extremes appear to be clustered in time with a series of similar events.

Flow Field

Since the inflow and the structural loads are time-synchronized, a detailed examination of the inflow conditions that produced these extremes can be made from the measured data. To illustrate this attribute of the LIST data, consider the extreme flap-bending load observed in the data set shown in Fig. 26b. The average hub-height wind speed in this record is 12.38 m/s with a turbulence intensity of 15.23 percent. The extreme occurs at approximately 23.7 seconds into the record and has a magnitude of 21.6 kNm. This extreme load is one of the largest flap loads in the bin class 5 wind speed.

The flap bending record for this event is shown in Fig. 29. Various measurements of the inflow at the time of the event are also shown in this figure. The time of the event has been delineated with a vertical dashed line in all of these records. For the inflow measurements, the position of the event has not been shifted forward in time to account for the transport time of approximately 2 seconds.^{††}

As seen in this figure, the horizontal wind speed component at the centerline of the turbine is well above the average wind speed for the ten-minute record. At the time of the event, the vertical wind speed component at the hub is reversing direction. The horizontal wind speed component is approximately 5 m/s less at the bottom of rotor than

^{††} The inflow instrumentation is located approximately 30.7 m in front of the turbine. Thus, with an average hub-height velocity of over 15 m/s, inflow events occur approximately 2 seconds before a measured structural event.

at the top, and approximately 2 m/s less of the right side of the rotor than on the left side. Thus, the rotor is seeing a strong shear field in both the horizontal and vertical directions, plus the vertical wind speed is oscillating between positive (up) and negative (down). Although this situation does not appear to be unique, even in the 20 seconds of data presented here, the result is a strong spike in the flap loads.

Timing

The data presented in Fig. 29 indicate that the conditions producing the extreme are prevalent for approximately 7 seconds. These conditions produce a succession of 5 strong spikes in the load histogram (at approximately 19, 22, 23, 24 and 26 seconds into the record). The extreme is the fourth spike in the succession. These peaks have magnitudes of 20.8, 19.8, 18.7, 21.6 and 18.8 kNm, respectively. Thus, extrema appear to be clustered in time.

From a fatigue standpoint, the clustering of extrema is not as important as the elapsed time between the largest loads and the smallest loads (over all data records). These are the peaks and valleys that are combined by the rainflow counting algorithm to form the large ranges found in the tail of the fatigue-cycle distribution shown in Figs. 19 and 20. Using the extreme load plot for the bin class 5 wind speeds shown in Fig. 26 and a similar plot of the extreme minimum values, the timing of the extreme fatigue cycles can be ascertained. In particular, the extreme maximum edge-bending load occurs approximately 43 hours before the extreme minimum edge-bending load. For flap-bending loads, the extreme maximum occurs approximately 94.5 hours before the extreme minimum. Thus, the extremes for edge and flap bending do not occur at the same time or even in the same ten-minute record.

CONCLUDING REMARKS

The long-term data set from the LIST program is used to examine the structural response of the Micon wind turbine to the inflow conditions that are representative of a Great Plains commercial site. Both short and long term loads are examined. Long-term fatigue loads are analyzed, and the correlation between inflow parameters and fatigue loads are quantified. The distribution of extreme loads on a turbine is examined, and the inflow conditions that produce these extremes are discussed. The analysis of inflow parameters and equivalent fatigue loads illustrate that the vertical component of inflow velocity and the Richardson Number consistently have the most influence on the fatigue spectrum. Long-term fatigue spectra illustrate that extrapolations of relatively short-term data are consistent with long-term measured data. Extreme operational loads are characterized using Gumbel distributions. A detailed examination of one of the largest extremes illustrates that the extreme loads are clustered in time and that there does not appear to be an extraordinary inflow event producing them.

ACKNOWLEDGEMENTS

The data used in this analysis is the direct results of a dedicated team of researchers. The personnel (including the author) and their primary duties in the LIST project are: Henry Dodd: Program Manager, SNL; Nolan Clark: Program Director, USDA-ARS; Herb Sutherland: Project Leader, SNL; Byron Neal: Site Engineer, USDA-ARS; Perry Jones: Site Engineer, SNL; Dale Berg and Jose Zayas: Data Acquisition System, SNL; Mark Rumsey: Data Analysis System, SNL; Tom Ashwill: Construction and Foundation Design, SNL; Clint Sanders: Student Assistant, USDA-ARS. The author wishes to thank the LIST Team for their efforts and support. The author also wishes to thank Neil Kelley, NREL, for supplying many of the discretized formulations for the various inflow variables presented in Appendix A.

REFERENCES

1. Sutherland, H.J., P.L. Jones, and B. Neal, 2001, "The Long-Term Inflow and Structural Test Program," *2001 ASME Wind Energy Symposium*, AIAA/ASME, pp. 162-172.
2. Sutherland, H.J., 2001, "Preliminary Analysis of the Structural And Inflow Data From the LIST Turbine," *2001 ASME Wind Energy Symposium*, AIAA/ASME, pp. 173-183.
3. Sutherland, H.J., 2002, "Inflow and the Fatigue of the LIST Wind Turbine," *2002 ASME Wind Energy Symposium*, AIAA/ASME, pp. 427-437.
4. Madsen, P.H., K. Pierce and M. Buhl, 1999, "Predicting Ultimate Loads for Wind Turbine Design," *1999 ASME Wind Energy Symposium*, p. 355.
5. Sutherland, H.J., and C.P. Butterfield., 1994 "A Summary of the Workshop on Fatigue Life Methodologies for Wind Turbines," *Proceedings of Windpower '94*, AWEA, Washington, DC, May.
6. *Mounturb Final Report*, 1996, G. Glinou and A. Fragoulis, eds., 3 vols., JOU2-CT93-0378.
7. Jones, P.L., H.J. Sutherland and B.A. Neal, 2001, *LIST/BMI Turbines, Instrumentation and Infrastructure*, SAND2001-1642, Sandia National Laboratories, Albuquerque, NM, 69 p.
8. Tangler, J., 1999, private communication.
9. O'Gorman, C.C., T.W. Simmermacher, 1999, *SERI Wind Turbine Blade (B3) Mass Properties Testing, Bushland, TX*, Internal SNL Memo, Sandia National Laboratories, Albuquerque, July 16.
10. Simmermacher, T., C. O'Gorman, W. Martin and F. Lopez, 1999, *Modal Test of SERI-Blade B1*, Internal SNL Memo, Sandia National Laboratories, Albuquerque, July 22.
11. Simmermacher, T. and T. Carne, 1999, *Tower Modal Survey*, Internal SNL Memo, Sandia National Laboratories, Albuquerque, December 20.
12. Tangler, J., B. Smith, N. Kelley and D. Jager, 1991, "Measured and Predicted Rotor Performance for the SERI Advanced Wind Turbine Blades," *Proceedings of Windpower '91*, SERI/TP-253-4673, Solar Energy Research Institute, Golden, CO, p. 104.
13. Tangler, J., B. Smith, D. Jager, and T. Olsen, 1990, *Atmospheric Performance of the SERI Thin-Airfoil Family*, SERI/TP-257-3939, Solar Energy Research Institute, Golden, CO.

14. Tangler, J., B. Smith, D. Jager, E. McKenna and J. Allread, 1989, "Atmospheric Performance Testing of the Special-Purpose SERI Thin Airfoil Family: Preliminary Results," *Proceedings of Windpower '89*, SERI/TP-257-3628, Solar Energy Research Institute, Golden, CO, p. 115.
15. Berg, D., and J. Zayas, 2001, "Accurate Time-Linked Data Acquisition System Field Deployment and Operational Experience," *2001 ASME Wind Energy Symposium*, AIAA/ASME, pp. 153-161.
16. Rohatgi, J.S., and V. Nelson, 1994, *Wind Characteristics, An Analysis for the Generation of Wind Power*, Alternative Energy Institute, Canyon, TX, 237 p.
17. Fragoulis, A.N., 1997, "The Complex Terrain Wind Environment and Its Effects on the Power Output and Loading of Wind Turbines," *1997 ASME Wind Energy Symposium*, AIAA/ASME, pp. 33-40.
18. Kelley, N.D., and H.E. McKenna, 1996, "The Evaluation of a Turbulent Loads Characterization System," *1996 ASME Wind Energy Symposium*, ASME, pp. 69-77.
19. Kelley, N.D., A.D. Wright, M.L. Buhl, Jr., and J.L. Tangler, 1997, "Long-Term Simulation of Turbulence-Induced Loads Using the SNL WIND-3D, FAST, YawDyn, and ADAMS Numerical Codes," *1997 ASME Wind Energy Symposium*, ASME, pp. 74-85.
20. Buhl, M.L., Jr., 2001, *CRUNCH User's Guide*, Ver. 2.61, NREL/NWTC, Golden, CO, 11 p.
21. Sutherland, H.J., 1999, *On the Fatigue Analysis of Wind Turbines*, SAND99-0089, Sandia National Laboratories, Albuquerque, NM, 132 p.
22. *Wind Turbine Generator Systems, Part 13: Measurement of Mechanical Loads*, Draft Technical Report, 1998, IEC 61400-13, prepared by IEC-TC88, Working Group 11.
23. Musial, W., M. Clark, N. Egging and M. Zuteck, 1997, "A Comparison of Strength and Load-Based Methods for Testing Wind Turbine Blades," *1997 ASME Wind Energy Symposium*, AIAA/ASME, W. Musial and D.E. Berg, eds., p. 228.
24. Press, W.H., S.A Teukolsky, W. T. Vetterling and B.P. Flannery, 1992, *Numerical Recipes in C, The Art of Scientific Computing*, Second Edition, Chapter 15.4, Cambridge University Press.
25. Madsen, P.H., K. Pierce and M. Buhl, 1999, "Predicting Ultimate Loads for Wind Turbine Design," *1999 ASME Wind Energy Symposium*, AIAA/ASME, T. Ashwill, ed., p. 355.
26. Laino, D.J., and K.G. Pierce, 2000, "Evaluating Statistical Loads Extrapolation Methods," *2000 ASME Wind Energy Symposium*, AIAA/ASME, P. Migliore, ed., p. 424.

Appendix A

NOMENCLATURE

SYMBOLS

a Regression coefficients, see Eq. 3

$F()$ Cumulative density function, see Eq. 9

F_e Equivalent fatigue load, see Eq. 11

f_o Rotational frequency of the turbine

g Acceleration of gravity, 9.8 m/s^2

I Turbulence intensity (percent)

$$\frac{\sigma_u}{U} \quad [A-1]$$

$(KE)_{Tu}$ Turbulence kinetic energy,

$$\frac{1}{2} \left[(u')^2 + (v')^2 + (w')^2 \right] \quad [A-2]$$

L Obukhov length:

$$\frac{-\overline{\theta_s} u_*^3}{0.4 g (\overline{w' \theta_s'})} \quad [A-3]$$

L_u, L_v, L_w Turbulence length scales in the u , v , and w directions (m)

$$L_u = \overline{U_s} \int_0^T R_u(\tau) d\tau \quad [A-4]$$

M, N, P Counting indexes

m Material constant, exponent for the S-N curve

N_o Cycle to failure at load F_e , see Eq. 11

P Barometric pressure, (hPa) at height z_1

P_s Height corrected pressure

$$P_s = P_1 - \left[\frac{0.0341416 P_1}{\Theta_1 + 273.16} \right] (z_s - z_1) \quad [A-5]$$

R Autocorrelation function

Ri Gradient Richardson number:

$$\frac{g}{\theta_m} \frac{\Delta \theta}{(\Delta U)^2} \quad [A-6]$$

S Dependence Coefficient, see Eq. 8

t Time

T Total period of time

u, U Horizontal wind speeds (m/s)

u* Local friction velocity, (m/s)

$$- \left| \sqrt{u' w'} \right| \quad [A-7]$$

$\overline{u' w'}$,
 $\overline{u' v'}$,
 $\overline{v' w'}$ Reynolds stresses, (m²/s²)

v Instantaneous horizontal wind vector component, perpendicular to the average horizontal wind direction Φ_H (m/s)

w Instantaneous vertical wind vector component, perpendicular to the average total wind direction Φ_T (m/s)

x, x Independent variable in regression analysis, see Eq. 3

X Basis functions in regression analysis, see Eq. 3

y Dependent variable in regression analysis, see Eq. 3, measured value

\hat{y} Dependent variable in regression analysis, see Eq. 3, calculate value from curve fit

z Vertical height (m)

α Vertical wind shear exponent:

$$U_z / U_{Hub} = \left[z / z_{Hub} \right]^\alpha \quad [A-8]$$

α_E Scale parameter for the Gumbel distribution, see Eq. 10

β_E Location parameter for the Gumbel distribution, see Eq. 11

Δ Gradient over distance, see Eq. B-4

γ_E Euler's constant (0.5772)

ϕ Wind direction (degrees with-respect-to True North)

- Θ Temperature, °C
- θ Pressure-corrected absolute temperature, °K

$$\theta_s = (\Theta_s + 273.16) \left[\frac{1000}{P_s} \right]^{0.286} \quad [A-9]$$

- τ Integration parameter on time
- \mathcal{X} Merit function in regression analysis, see Eq. 3

SUBSCRIPTS

- 1, 2 Vertical positions 1 and 2
- H Horizontal
- i, j, k Counting indexes
- m Average over distance, see Eq. B-3
- T Total
- Tu Turbulence
- U Horizontal Wind Speed at Hub Height
- s Sonic

SUPERSCRIPTS

- ' Instantaneous value with the mean removed, see Appendix B

APPENDIX B

GENERAL EQUATIONS

\bar{X} Mean value of X over time period t:

$$\bar{X} = \frac{1}{T} \int_0^T x(\tau) d\tau = \frac{1}{N} \sum_{i=1}^N x_i \quad [B-1]$$

X' Fluctuation component of X:

$$x'(t) = x(t) - \bar{X} \quad [B-2]$$

X_m Mean over two elevations:

$$X_m = \frac{(X_1 + X_2)}{2} \quad [B-3]$$

ΔX Differential in the vertical direction:

$$\Delta X = \frac{X_2 - X_1}{z_2 - z_1} \quad [B-4]$$

σ_x Standard deviation;

$$\sqrt{\frac{1}{N} \sum_{i=1}^N [x_i']^2} = \sqrt{\frac{1}{N} \sum_{i=1}^N [x_i - \bar{X}]^2} \quad [B-5]$$

S_x Skewness;

$$\frac{\frac{1}{N} \sum_{i=1}^N [x_i']^3}{\sigma_x^3}, \quad [B-6]$$

K_x Kurtosis;

$$\frac{\frac{1}{N} \sum_{i=1}^N [x_i']^4}{\sigma_x^4} - 3, \quad [B-7]$$

LIST of Figures

- Fig. 1. The Micon 65/13M Turbine at the Bushland Test Site.
- Fig. 2. Site Diagram.
- Fig. 3. Schematic Diagram of the Inflow Instrumentation for the LIST Turbine.
- Fig. 4. Schematic Diagram of the Structural Instrumentation for the LIST Turbine.
- Fig. 5. Distribution of the Ten-Minute Data Records by Hub-Height Mean Wind Speed.
- Fig. 6. Typical Horizontal Wind Speed Data.
- Fig. 6a. First 100 seconds of the Data Record.
- Fig. 6b. First 20 seconds of the Data Record.
- Fig. 7. Typical Horizontal Wind Speed Direction.
- Fig. 7a. First 100 seconds of the Data Record.
- Fig. 7b. First 20 seconds of the Data Record.
- Fig. 8. Typical Vertical Wind Speed.
- Fig. 9. Instantaneous Reynolds Stress for the Horizontal and Vertical Velocity Components.
- Fig. 10. Horizontal Wind Speed from the Bottom to the Top of the Rotor.
- Fig. 11. Horizontal Wind Speed Across the Rotor Disk at Hub Height.
- Fig. 12. Edge-Bending Moment in the Root of Blade 1.
- Fig. 12a. First Ten Seconds of the Data Record.
- Fig. 12b. First Fifty Seconds of the Data Record.
- Fig. 13. Flap-Bending Moment in the Root of Blade 2.
- Fig. 13a. First Ten Seconds of the Data Record.
- Fig. 13b. First Fifty Seconds of the Data Record.
- Fig. 14. Typical Power Data for Turbines A and C.
- Fig. 15. Power Curve for the Three Micon 65/13M Turbines at the Bushland Site.
- Fig. 16. Power Coefficient for the Three Micon 65/13M Turbines at the Bushland Site.
- Fig. 17. Azimuth Averaged Edge-Bending Moment.
- Fig. 17a. Root Edge-Bending Moment in Blade 1.
- Fig. 17b. Blade Edge-Bending Moment in Blades 2 and 3, 40 percent Span.
- Fig. 18. Power Spectral Density for Blade Root Bending Moments.
- Fig. 18a. Root Edge-Bending Moment.
- Fig. 18b. Root Flap-Bending Moment

Fig. 19. Fatigue Load Spectrum for Bin Class 5 Wind Speeds.

Fig. 19a. Edge-Bending in the Root of Blade 1.

Fig. 19b. Flap-Bending in the Root of Blade 1.

Fig. 20. Exceedance Plots of the Fatigue Load Spectrum for Bin Class 5 Wind Speeds.

Fig. 20a. Edge-Bending in the Root of Blade 1.

Fig. 20b. Flap-Bending in the Root of Blade 2.

Fig. 21. Dependence of Equivalent Fatigue Load on Various Inflow Parameters for Bin Class 5 (11-13 m/s) Wind Speeds.

Fig. 21a. Flap Bending Loads.

Fig. 21b. Edge Bending Loads.

Fig. 22. Dependence of the Flap-Bending, Equivalent Fatigue Load on Various Inflow Parameters for Bin Class 4 Wind Speeds.

Fig. 23. Dependence of the Flap-Bending, Equivalent Fatigue Load on Various Inflow Parameters for Bin Class 6 Wind Speeds.

Fig. 24. Dependence of the Flap-Bending, Equivalent Fatigue Load on Various Inflow Parameters for Bin Class 7 Wind Speeds.

Fig. 25. Dependence of the Flap-Bending, Equivalent Fatigue Load on Various Inflow Parameters for Bin Class 8 Wind Speeds.

Fig. 26. Load Extremes for Bin Class 5 Wind Speeds.

Fig. 26a. Edge-Bending Loads.

Fig. 26b. Flap-Bending Loads.

Fig. 27. Gumbel Distribution of the Load Extremes for Bin Class 5 Wind Speeds.

Fig. 27a. Edge-Bending Loads.

Fig. 27b. Flap-Bending Loads.

Fig. 28. Gumbel Distribution of the Load Extremes for Bin Class 8 Wind Speeds.

Fig. 28a. Edge-Bending Loads.

Fig. 28b. Flap-Bending Loads.

Fig. 29. Flow Field and Structural Measurements about the Extreme Flap Event for Bin Class 5 Wind Speeds.

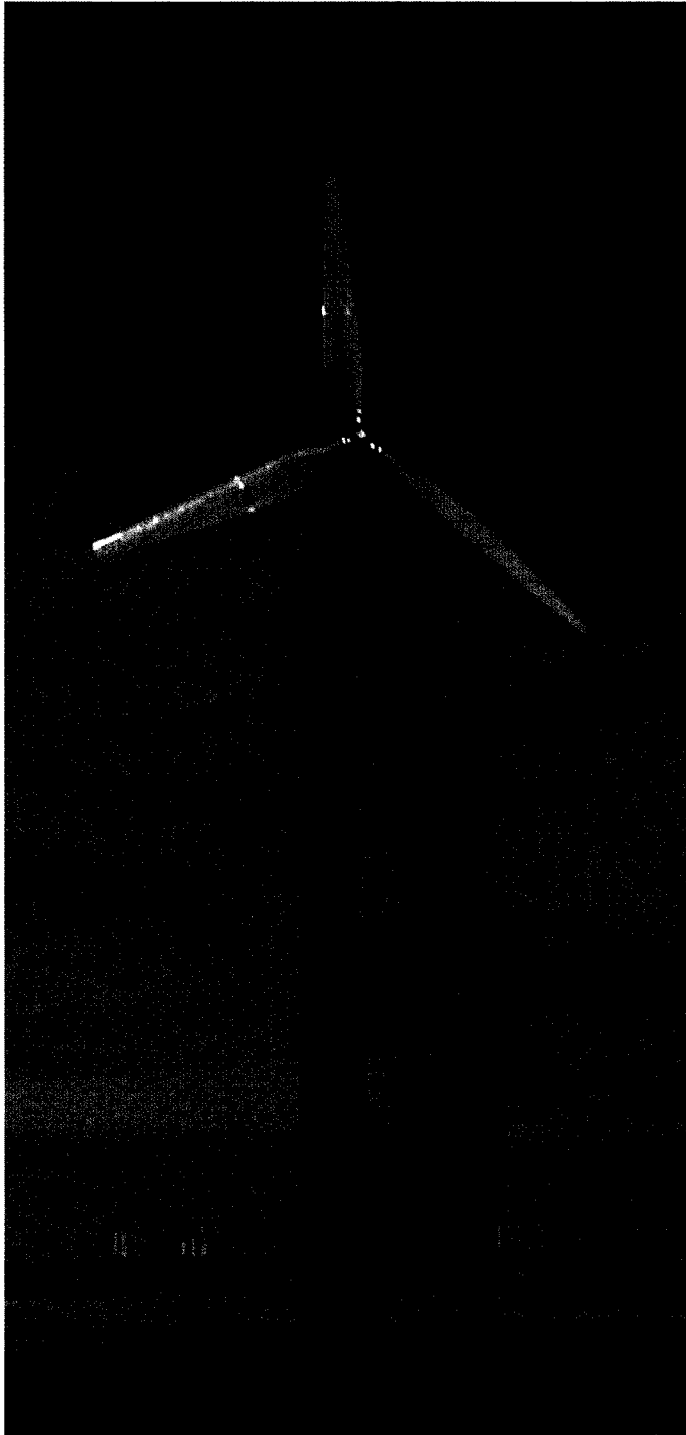


Fig. 1. The Micon 65/13M Turbine at the Bushland Test Site.

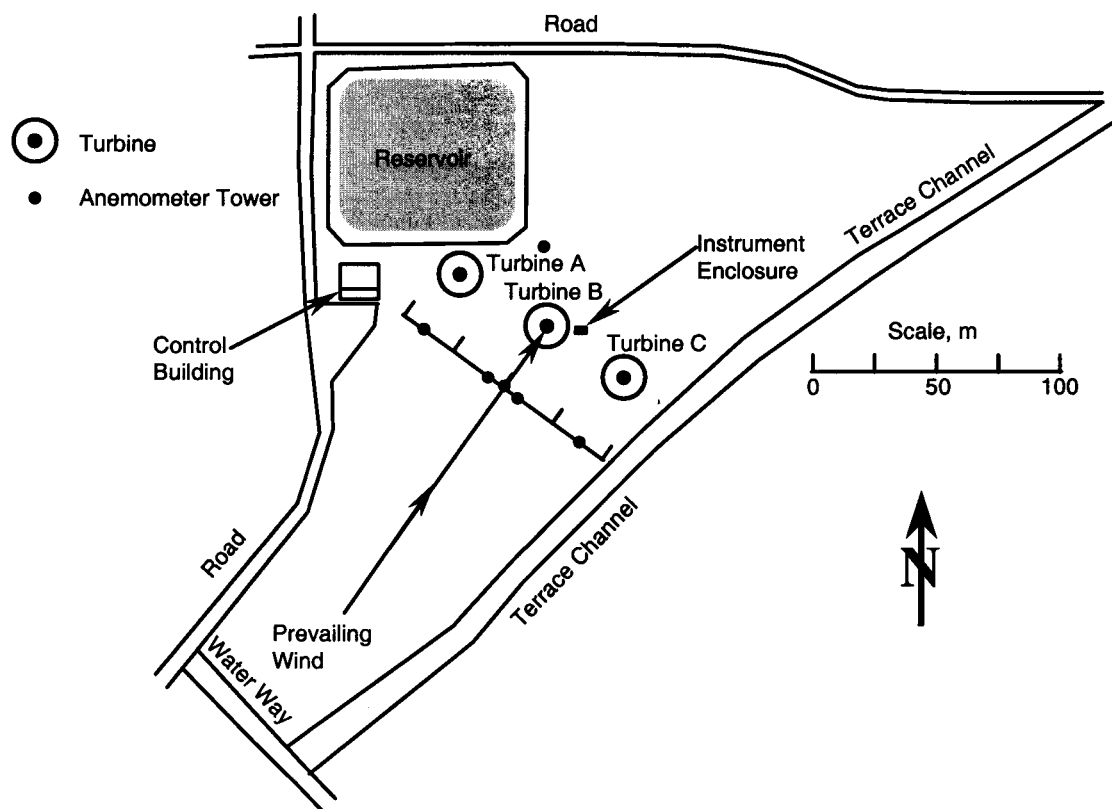


Fig. 2. Site Diagram.

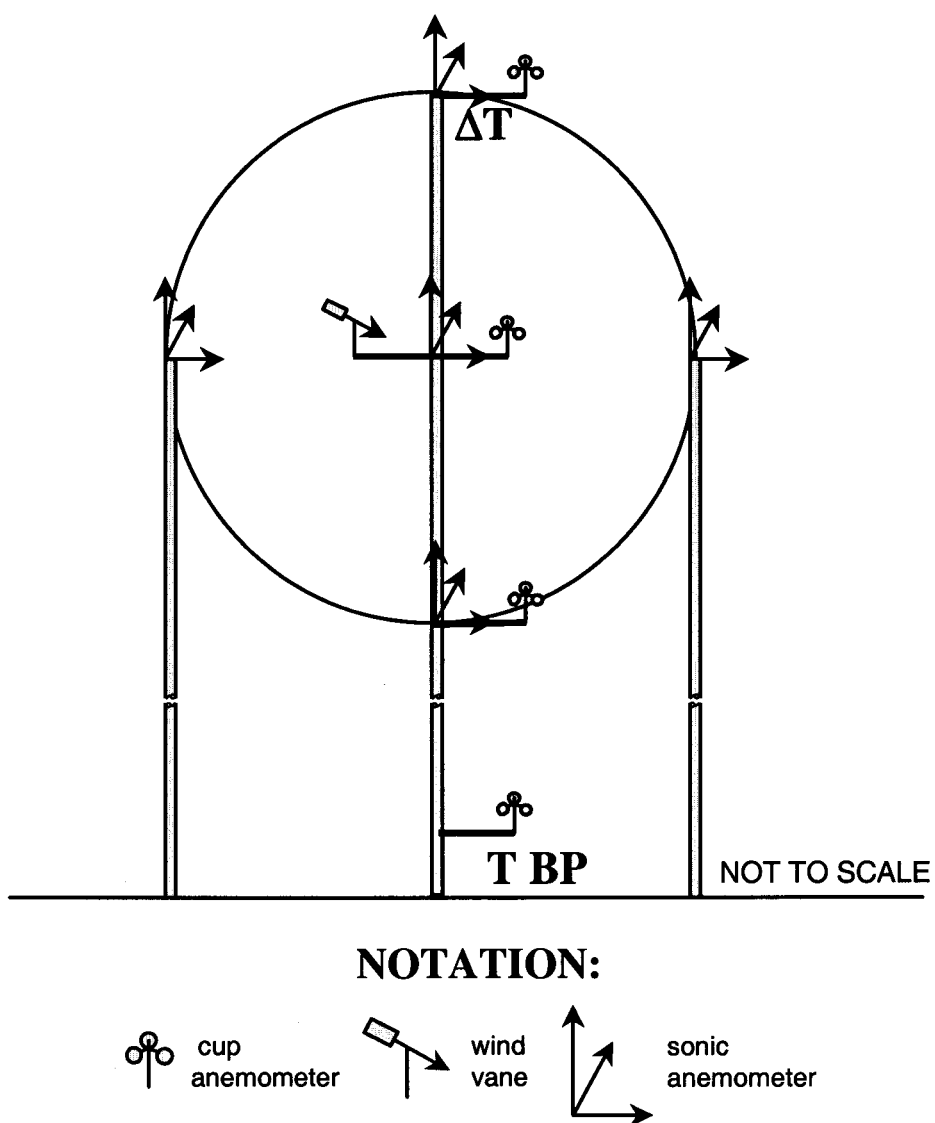


Fig. 3. Schematic Diagram of the Inflow Instrumentation for the LIST Turbine.

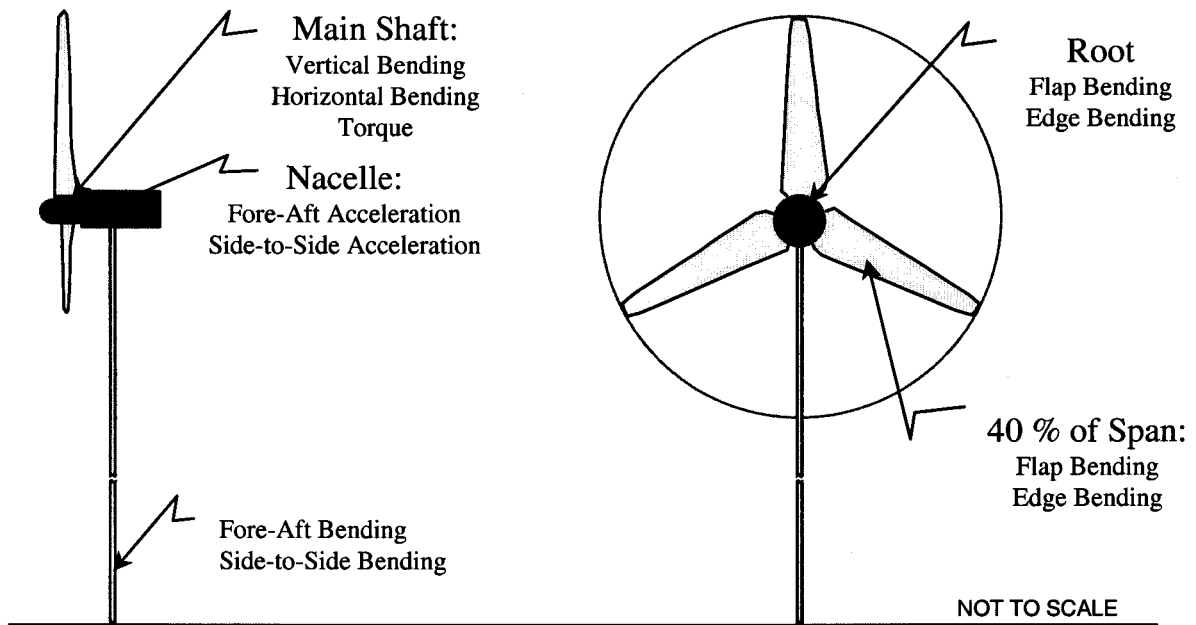


Fig. 4. Schematic Diagram of the Structural Instrumentation for the LIST Turbine.

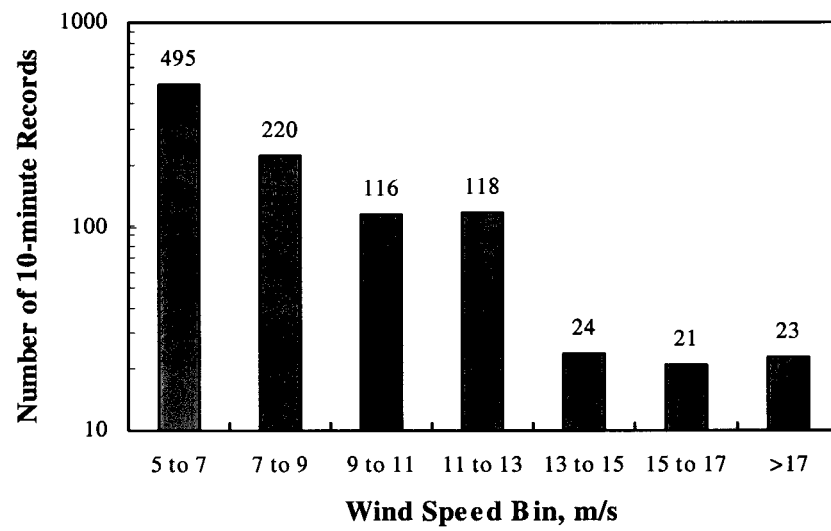


Fig. 5. Distribution of the Ten-Minute Data Records by Hub-Height Mean Wind Speed.

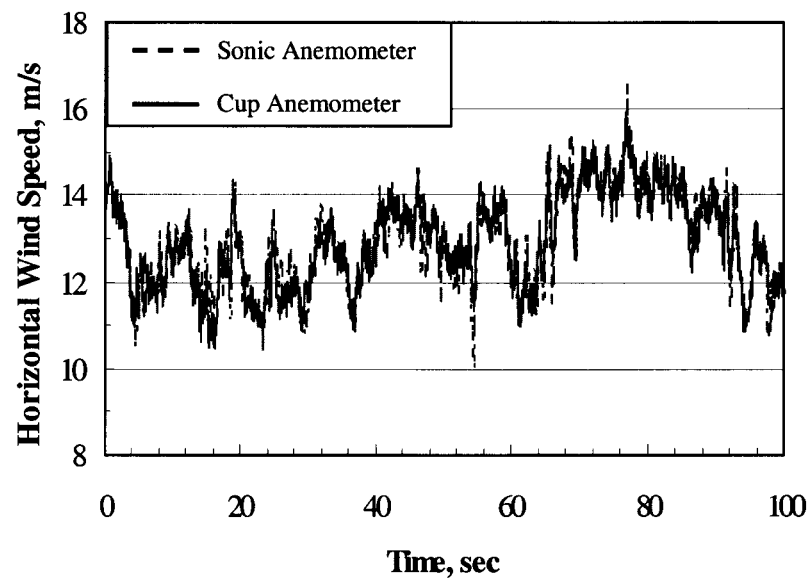


Fig. 6a. First 100 seconds of the Data Record.

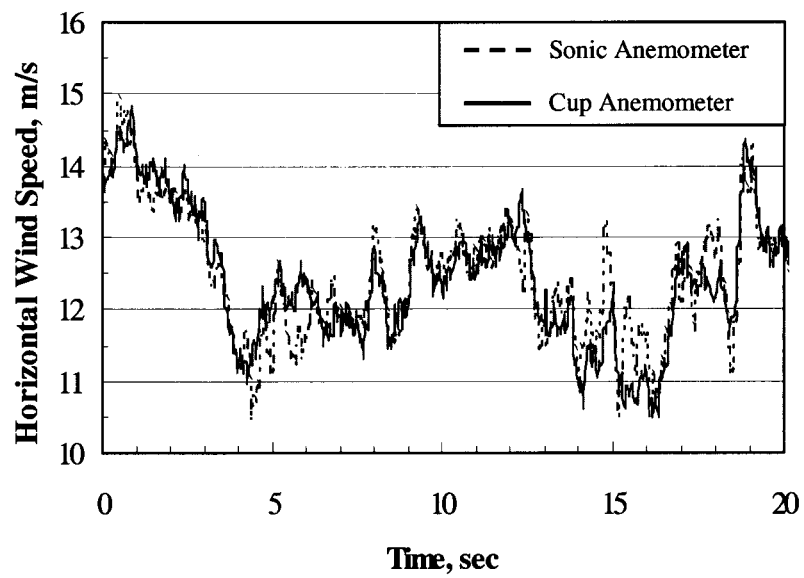


Fig. 6b. First 20 seconds of the Data Record.

Fig. 6. Typical Horizontal Wind Speed Data.

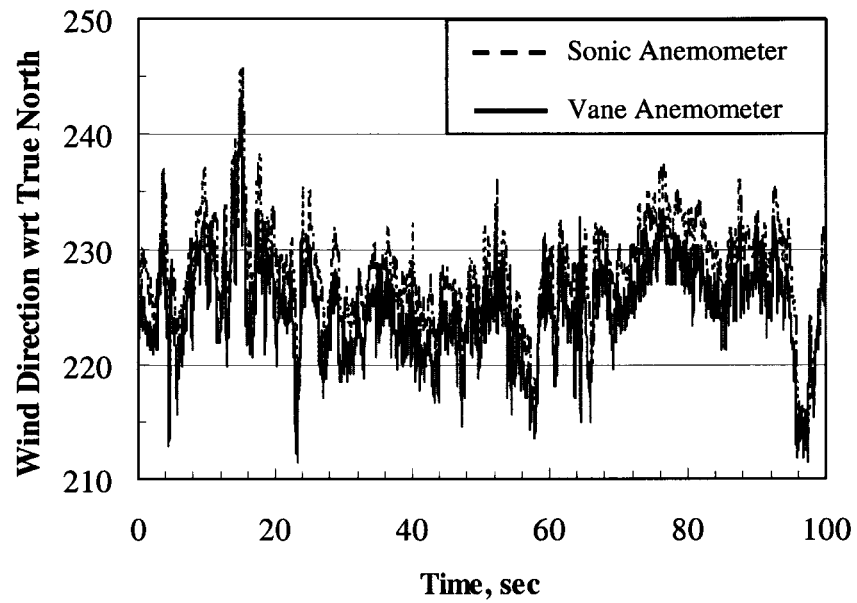


Fig. 7a. First 100 seconds of the Data Record.

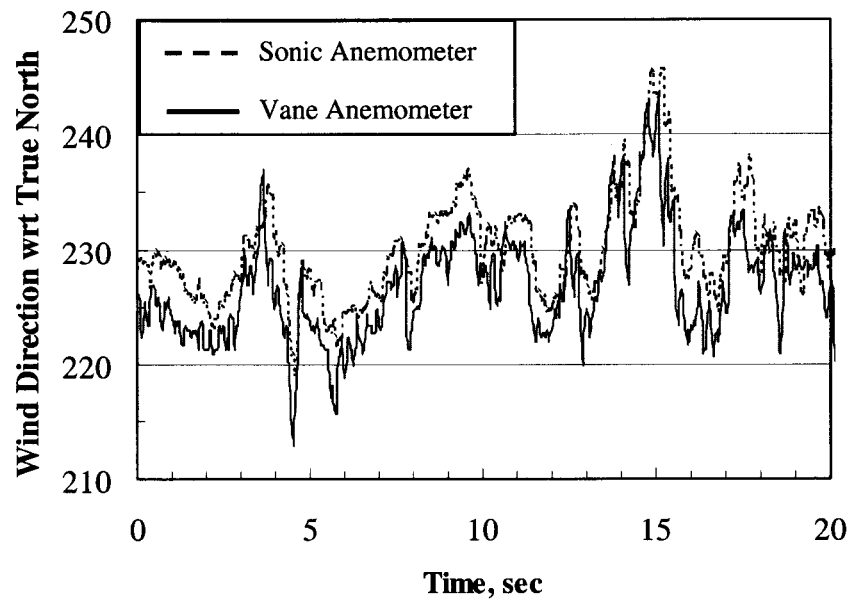


Fig. 7b. First 20 seconds of the Data Record.

Fig. 7. Typical Horizontal Wind Speed Direction.

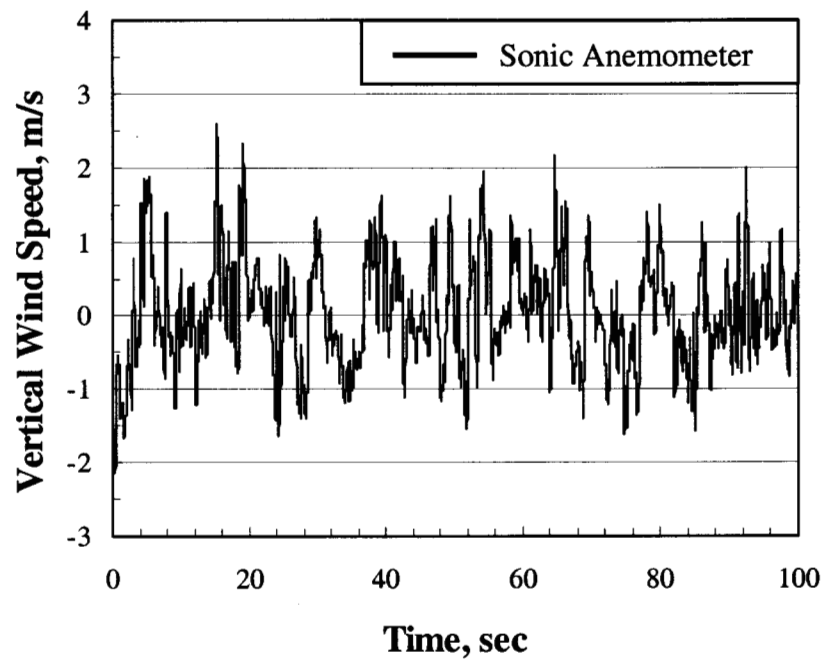


Fig. 8. Typical Vertical Wind Speed.

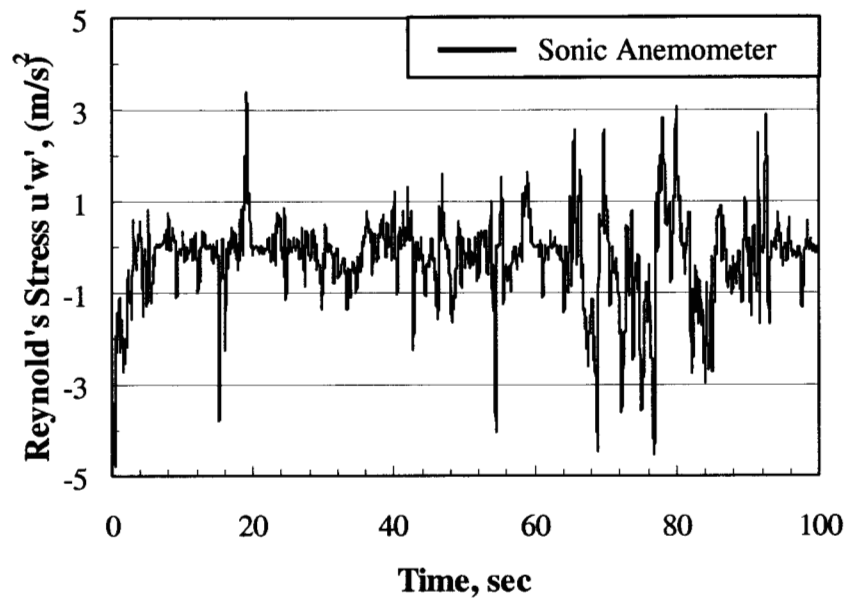


Fig. 9. Instantaneous Reynolds Stress for the Horizontal and Vertical Velocity Components.

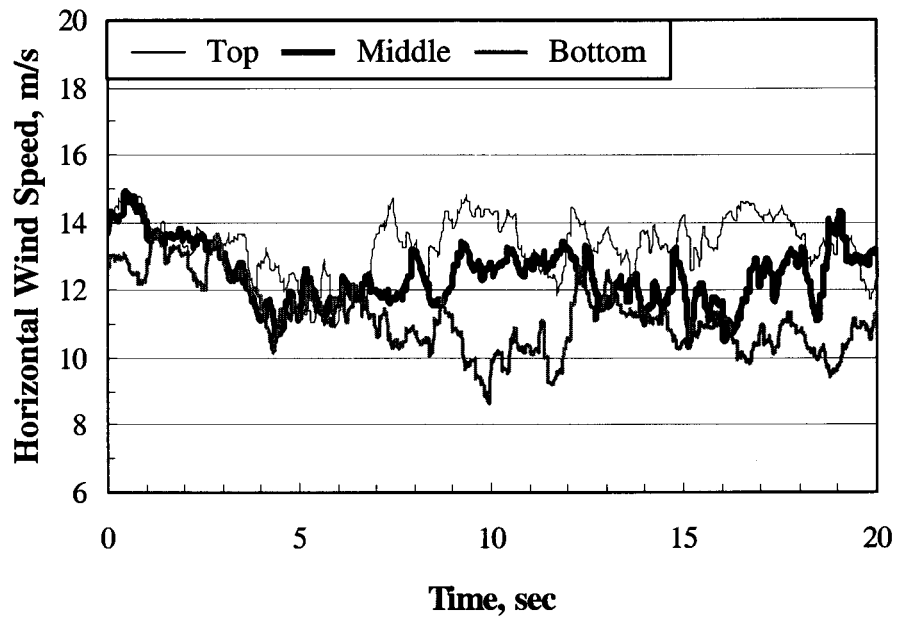


Fig. 10. Horizontal Wind Speed from the Bottom to the Top of the Rotor.

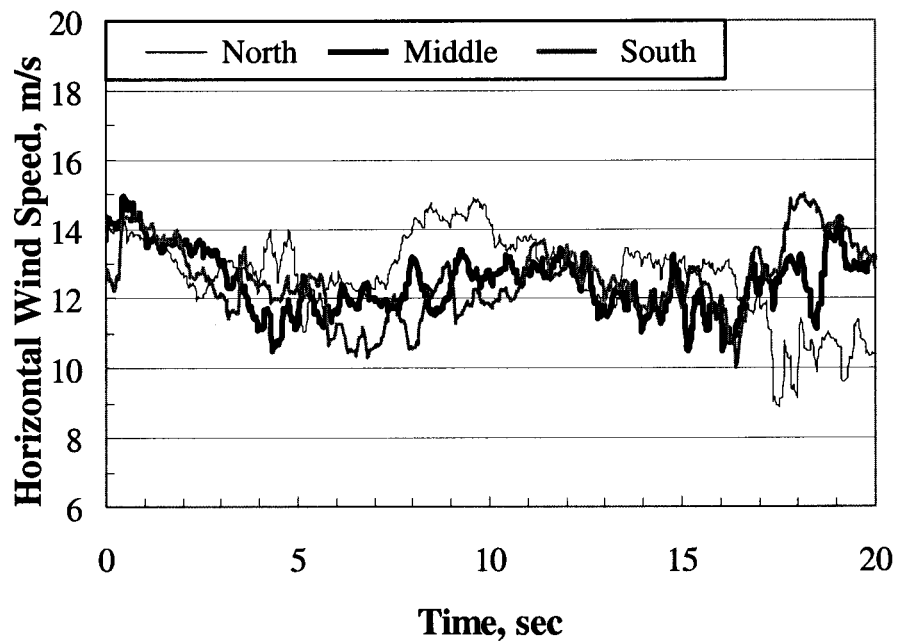


Fig. 11. Horizontal Wind Speed Across the Rotor Disk at Hub Height.

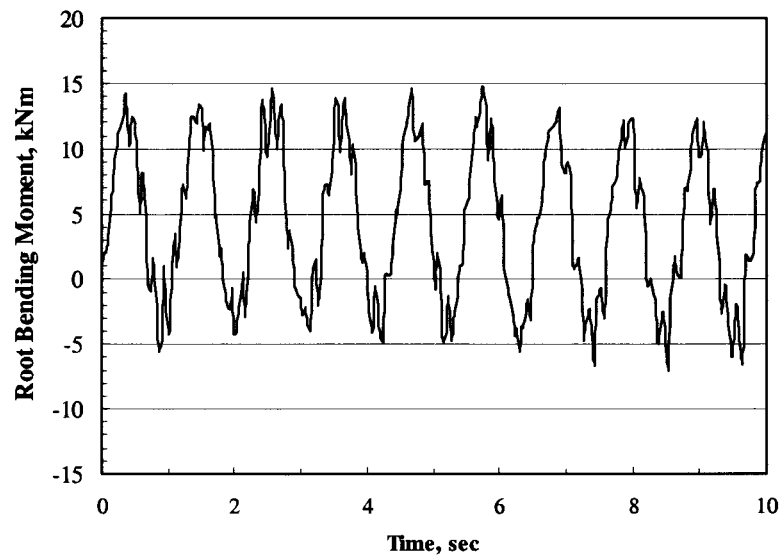


Fig. 12a. First Ten Seconds of the Data Record.

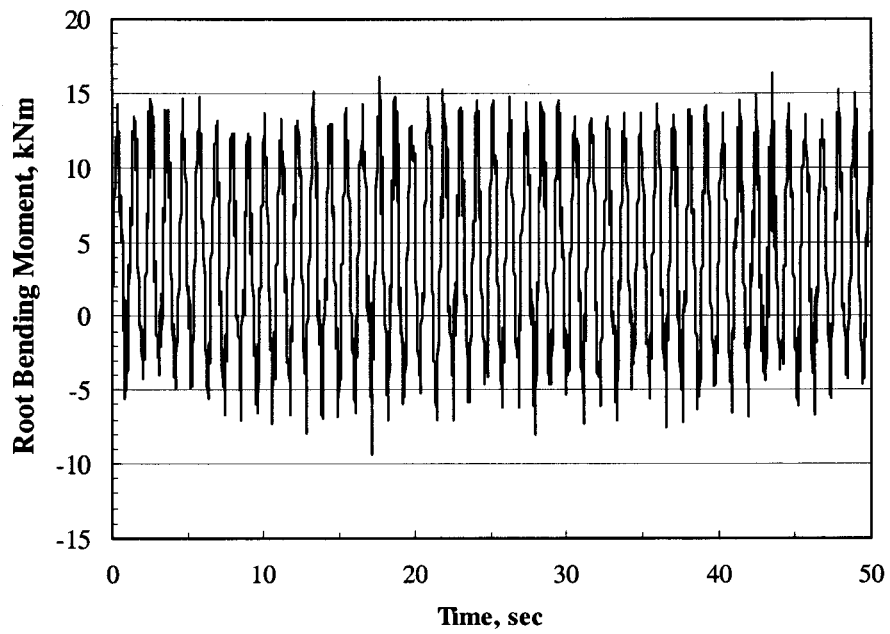


Fig. 12b. First Fifty Seconds of the Data Record.

Fig. 12. Edge-Bending Moment in the Root of Blade 1.

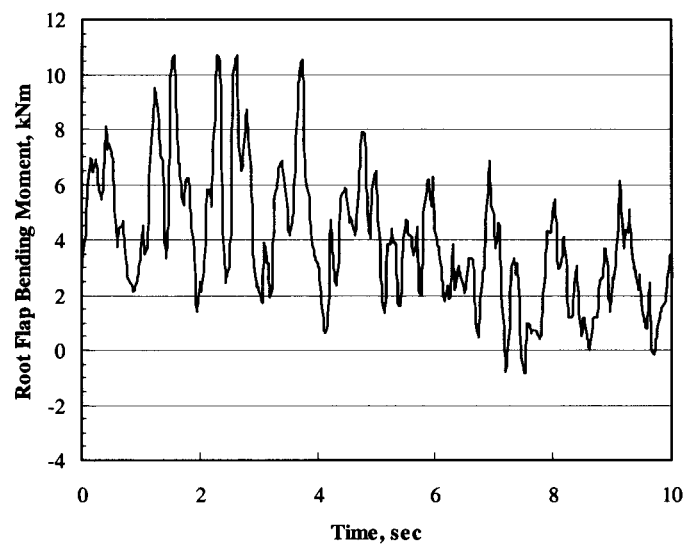


Fig. 13a. First Ten Seconds of the Data Record.

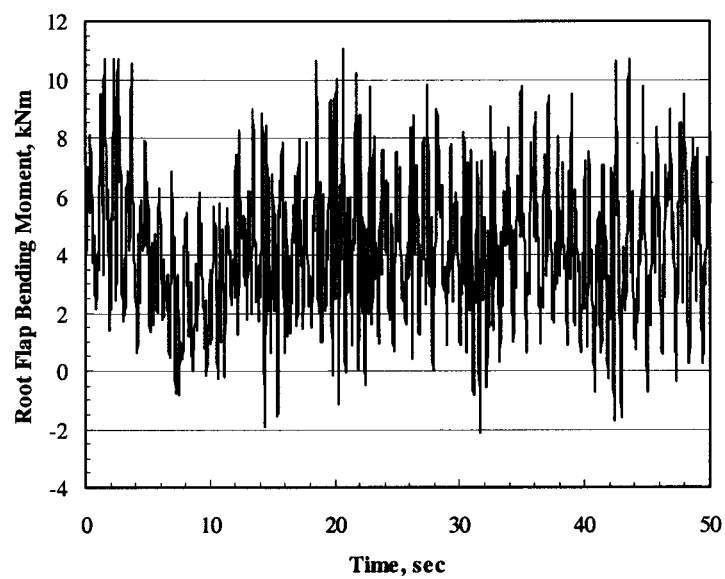


Fig. 13b. First Fifty Seconds of the Data Record.

Fig. 13. Flap-Bending Moment in the Root
of Blade 2.

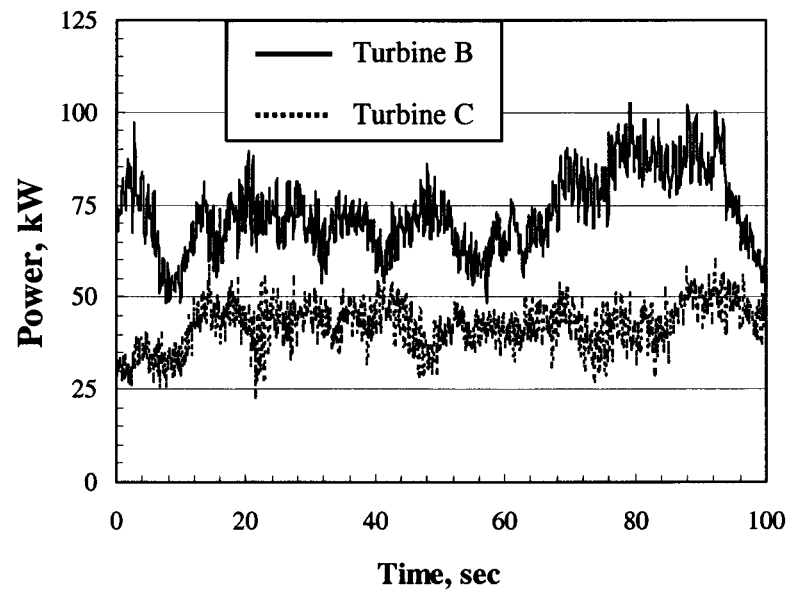


Fig. 14. Typical Power Data for Turbines A and C.

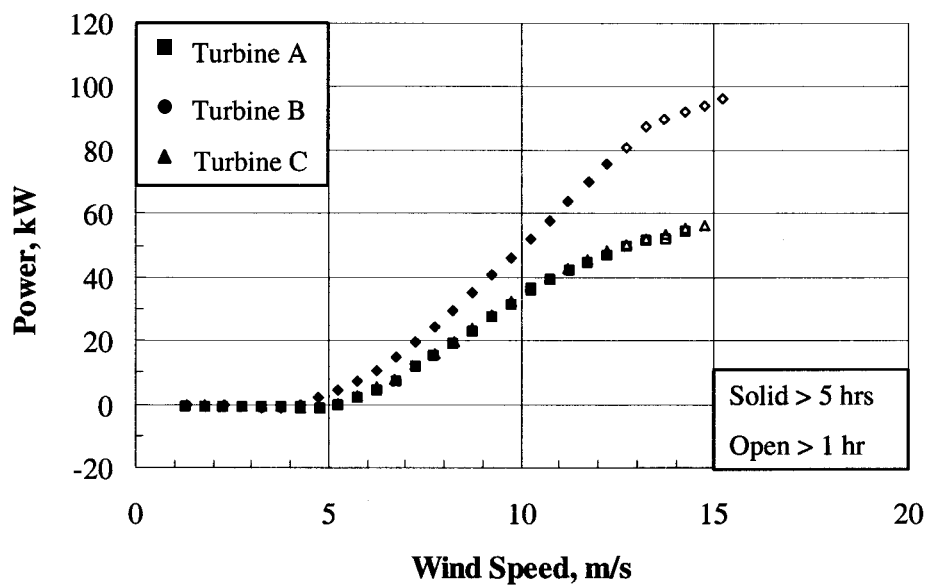


Fig. 15. Power Curve for the Three Micon 65/13M Turbines at the Bushland Site.

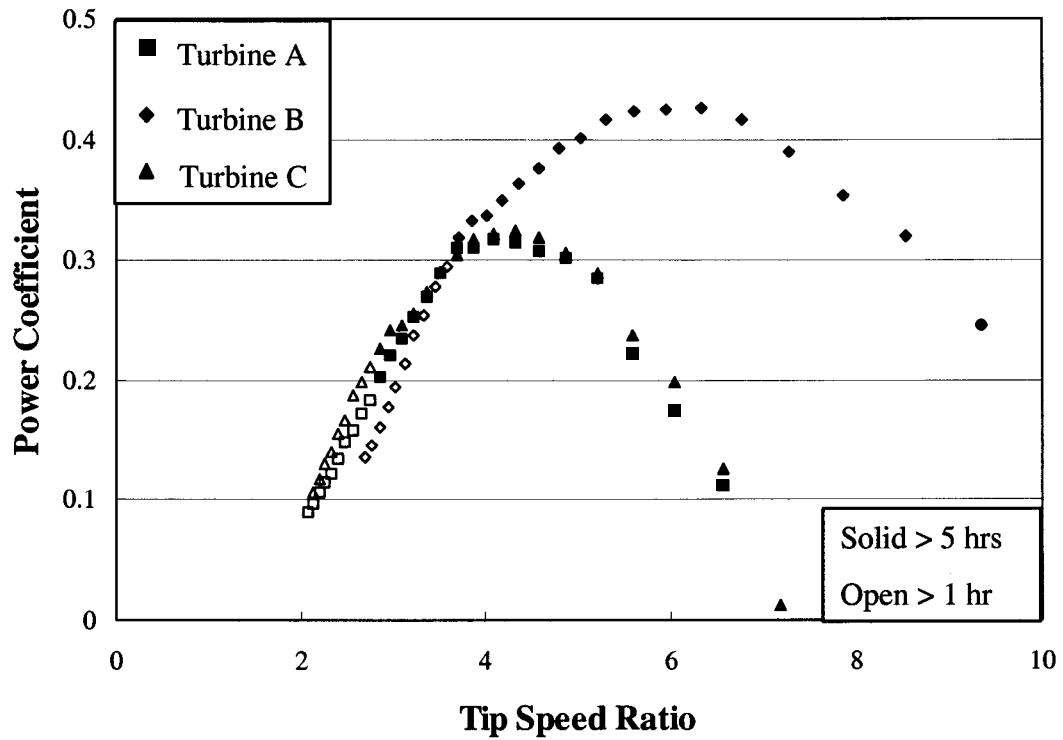


Fig. 16. Power Coefficient for the Three Micon 65/13M Turbines at the Bushland Site.

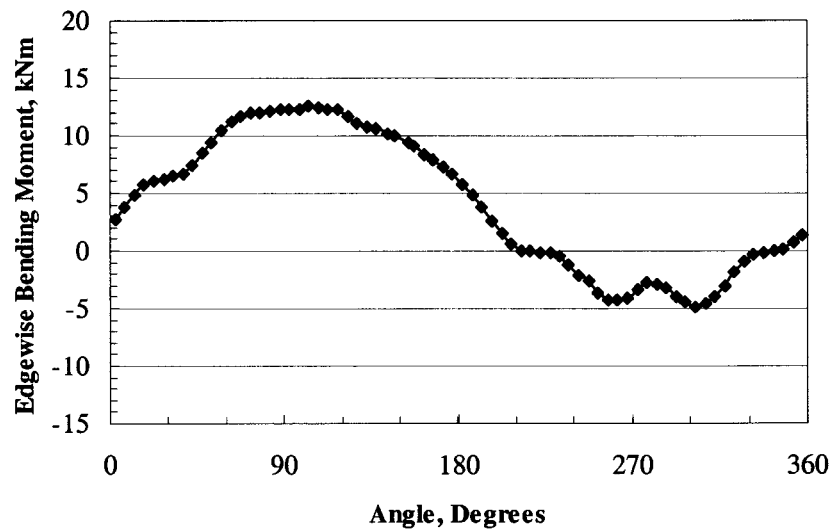


Fig. 17a. Root Edge-Bending Moment in Blade 1.

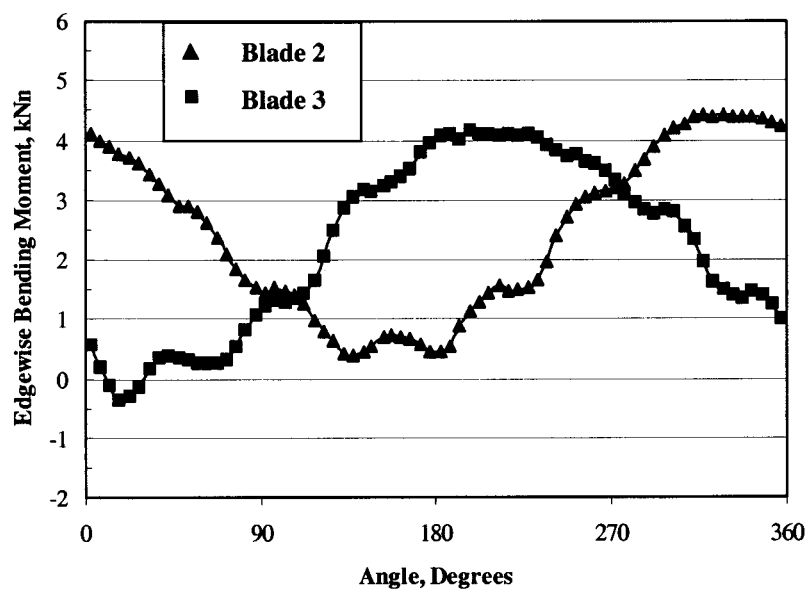


Fig. 17b. Blade Edge-Bending Moment in Blades 2 and 3, 40 percent Span.

Fig. 17. Azimuth Averaged Edge-Bending Moment.

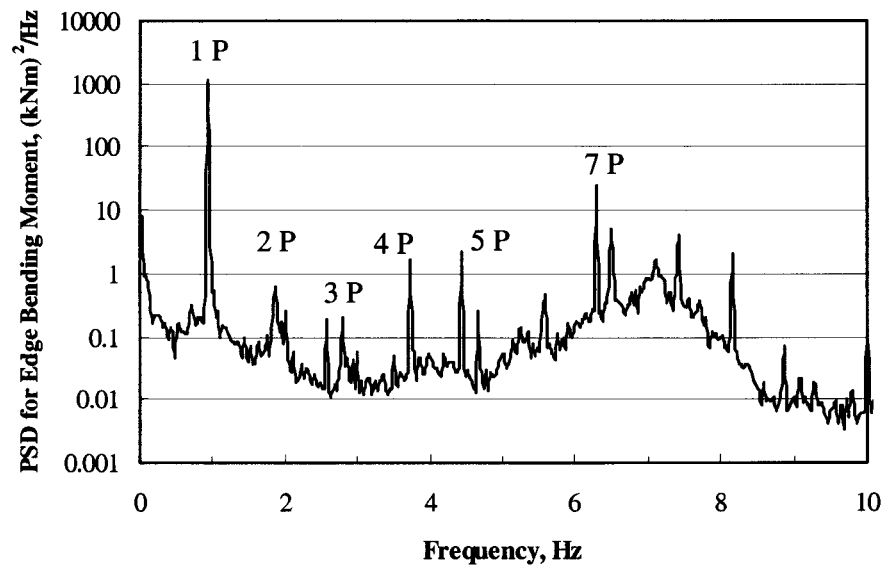


Fig. 18a. Root Edge-Bending Moment.

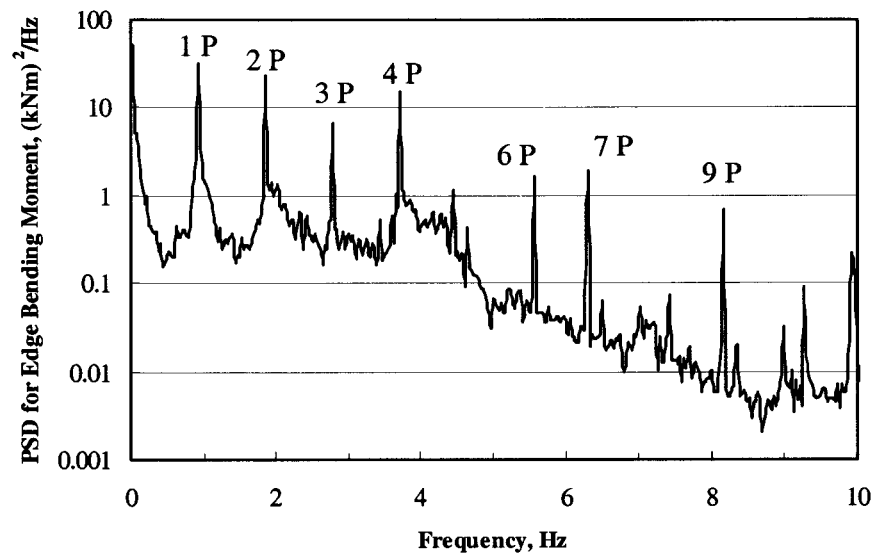


Fig. 18b. Root Flap-Bending Moment

Fig. 18. Power Spectral Density for Blade Root Bending Moments.

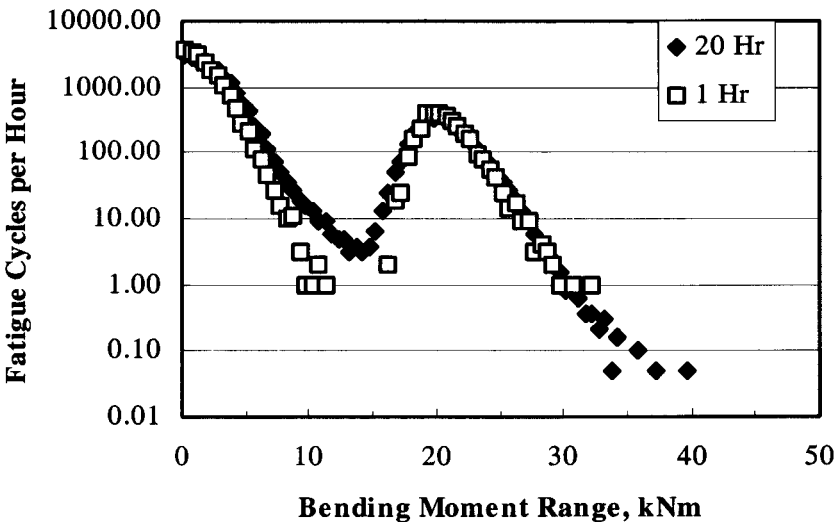


Fig. 19a. Edge-Bending in the Root of Blade 1.

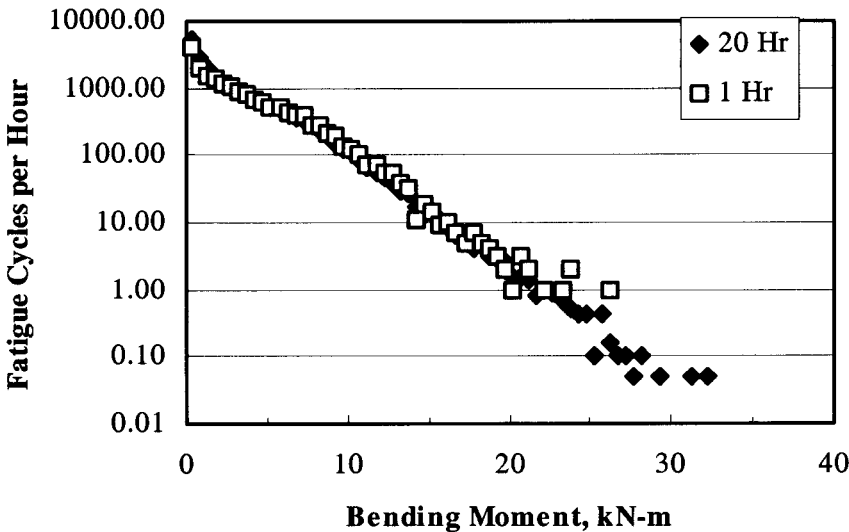


Fig. 19b. Flap-Bending in the Root of Blade 1.

Fig. 19. Fatigue Load Spectrum for Bin Class 5 Wind Speeds.

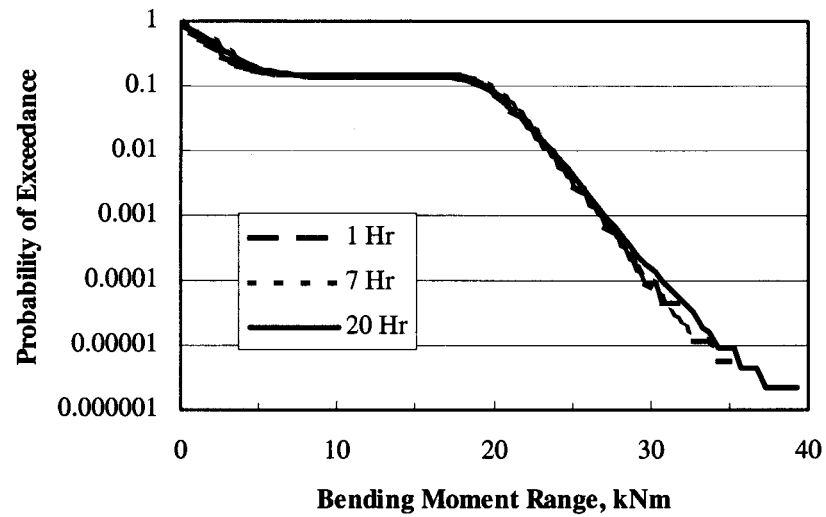


Fig. 20a. Edge-Bending in the Root of Blade 1.

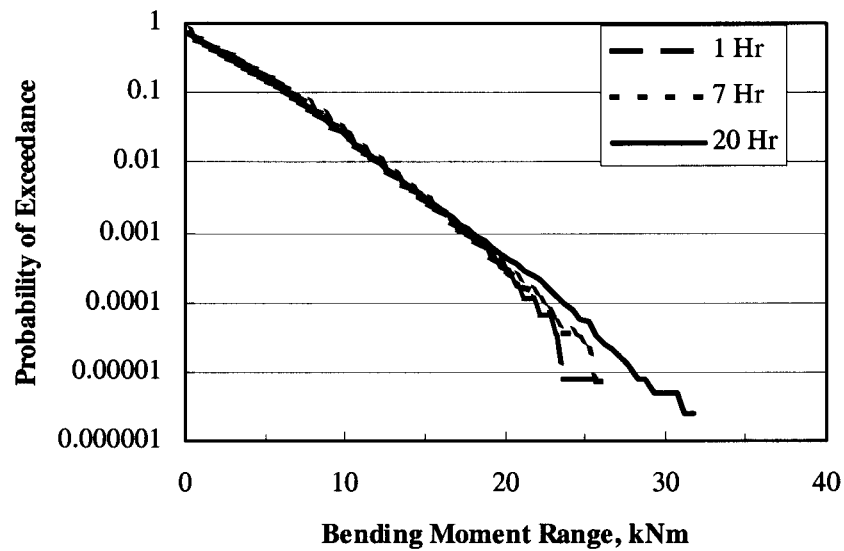


Fig. 20b. Flap-Bending in the Root of Blade 2.

Fig. 20. Exceedance Plots of the Fatigue Load Spectrum for Bin Class 5 Wind Speeds.

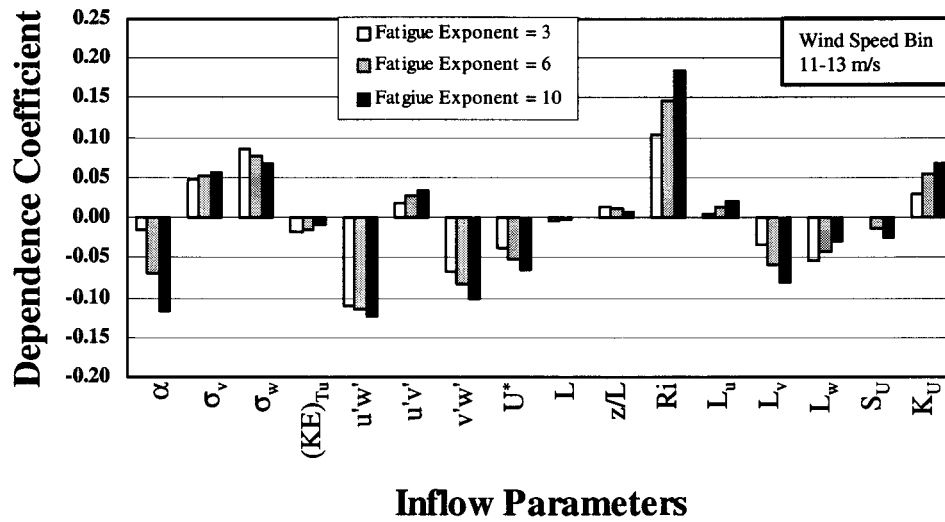


Fig. 21a. Flap Bending Loads.

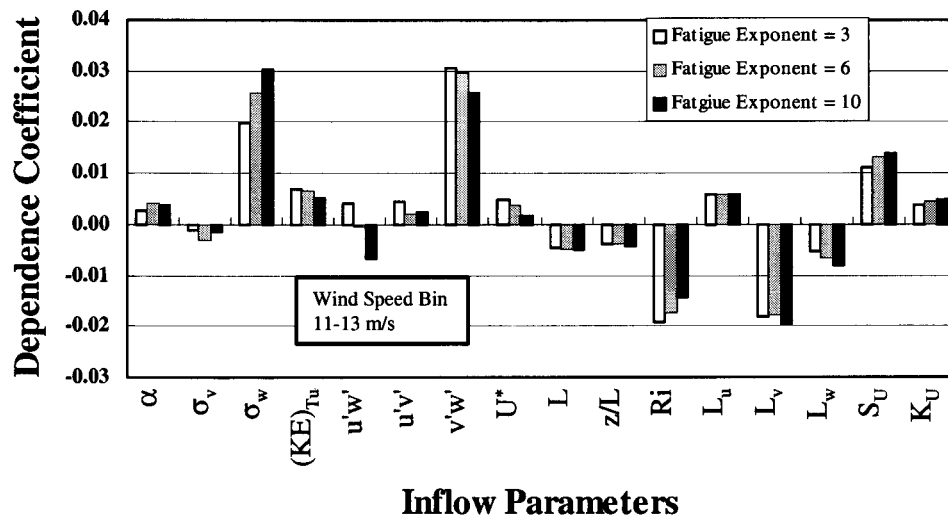


Fig. 21b. Edge Bending Loads.

Fig. 21. Dependence of Equivalent Fatigue Load on Various Inflow Parameters for Bin Class 5 (11-13 m/s) Wind Speeds.

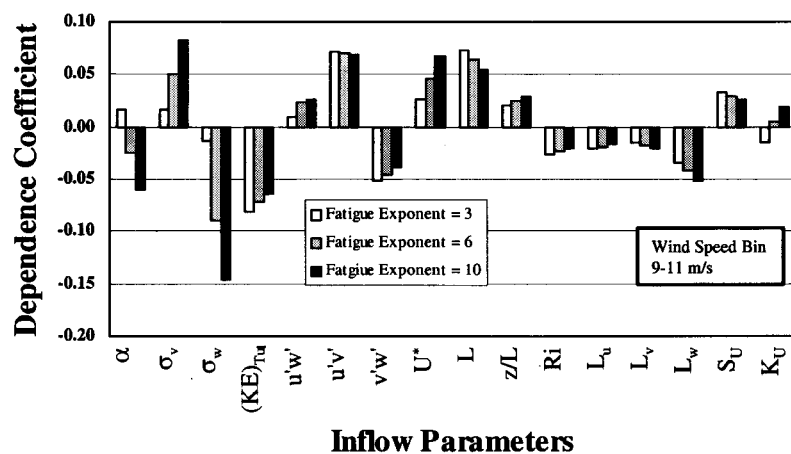


Fig. 22. Dependence of the Flap Bending, Equivalent Fatigue Load on Various Inflow Parameters for Bin Class 4 Wind Speeds.

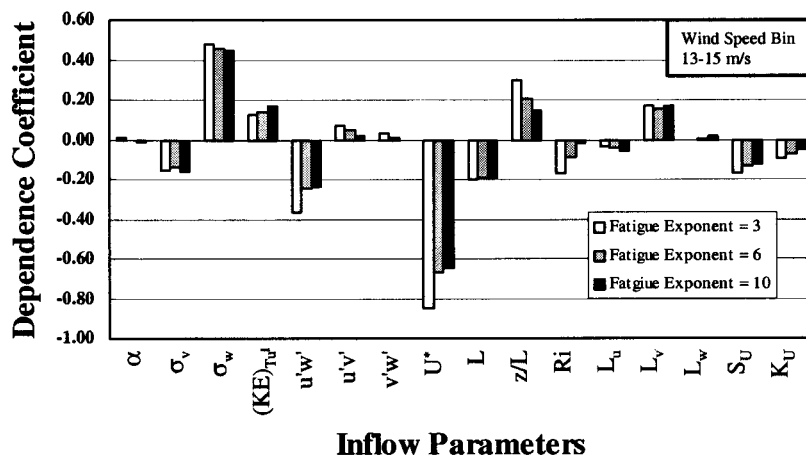


Fig. 23. Dependence of the Flap Bending, Equivalent Fatigue Load on Various Inflow Parameters for Bin Class 6 Wind Speeds.

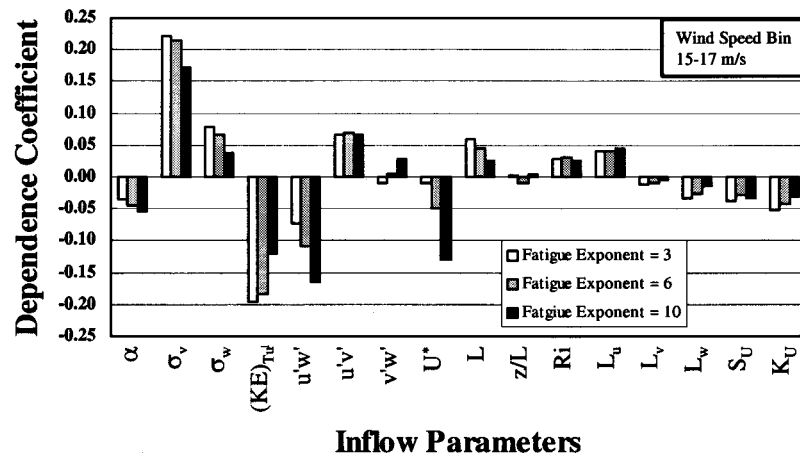


Fig. 24. Dependence of the Flap Bending, Equivalent Fatigue Load on Various Inflow Parameters for Bin Class 7 Wind Speeds.

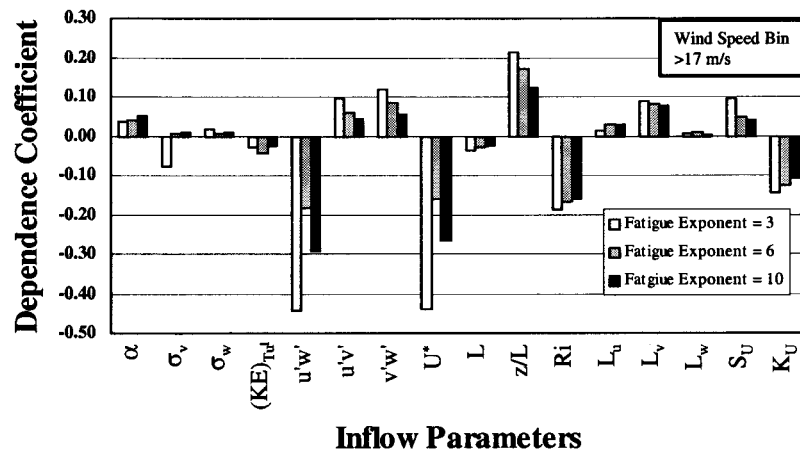


Fig. 25. Dependence of the Flap Bending, Equivalent Fatigue Load on Various Inflow Parameters for Bin Class 8 Wind Speeds.

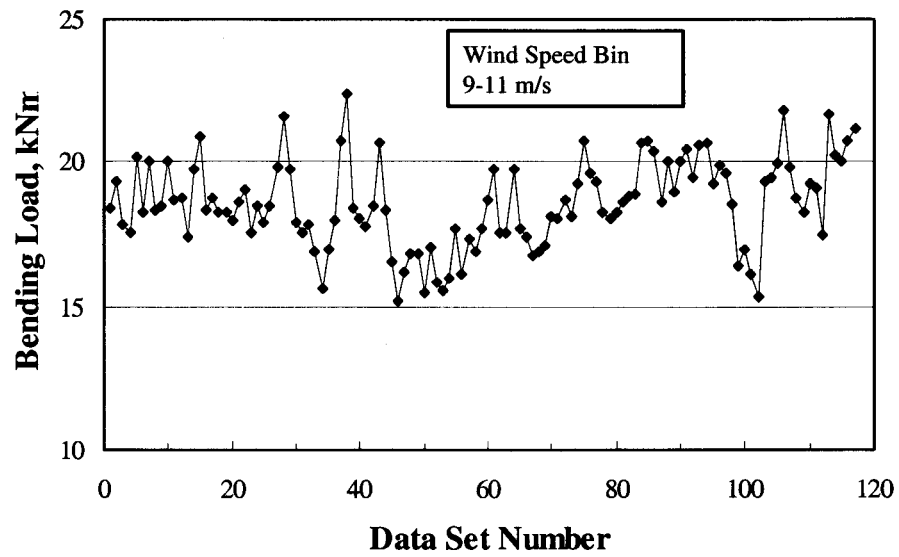


Fig. 26a. Edge-Bending Loads.

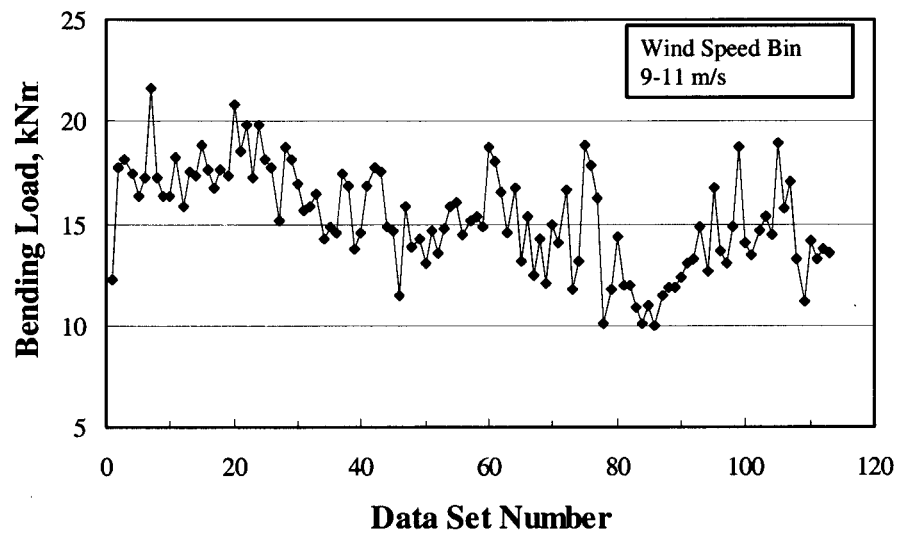


Fig. 26b. Flap-Bending Loads.

Fig. 26. Load Extremes for Bin Class 5 Wind Speeds.

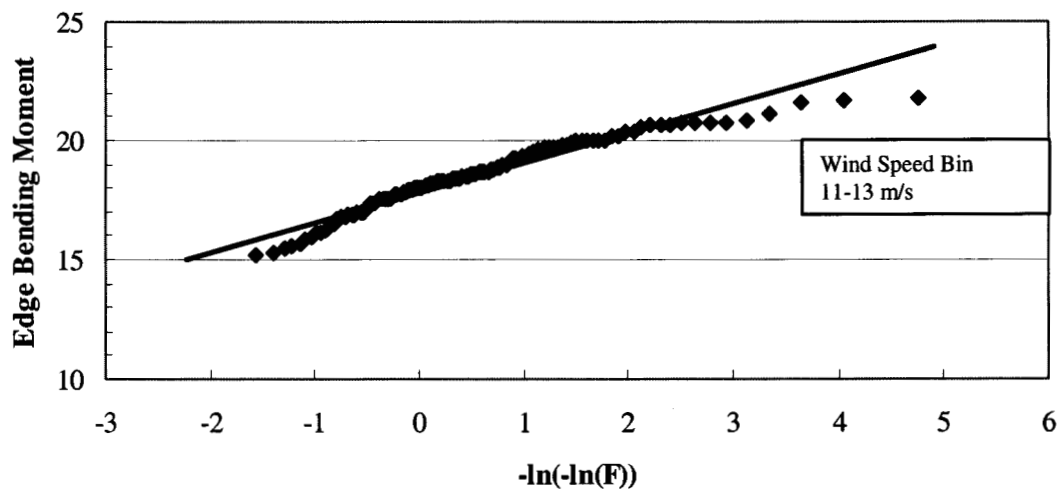


Fig. 27a. Edge-Bending Loads.

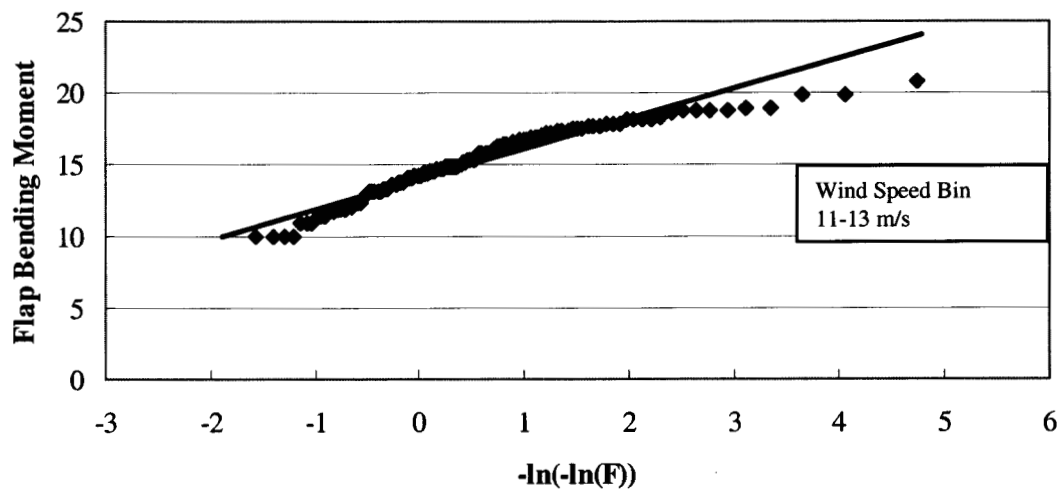


Fig. 27b. Flap-Bending Loads.

Fig. 27. Gumbel Distribution of the Load Extremes for Bin Class 5 Wind Speeds.

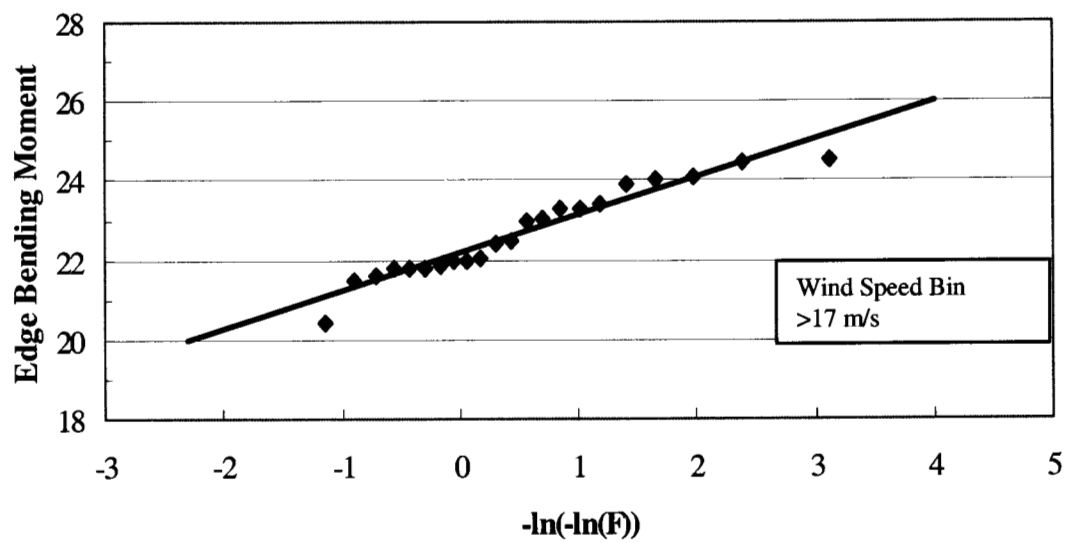


Fig. 28a. Edge-Bending Loads.

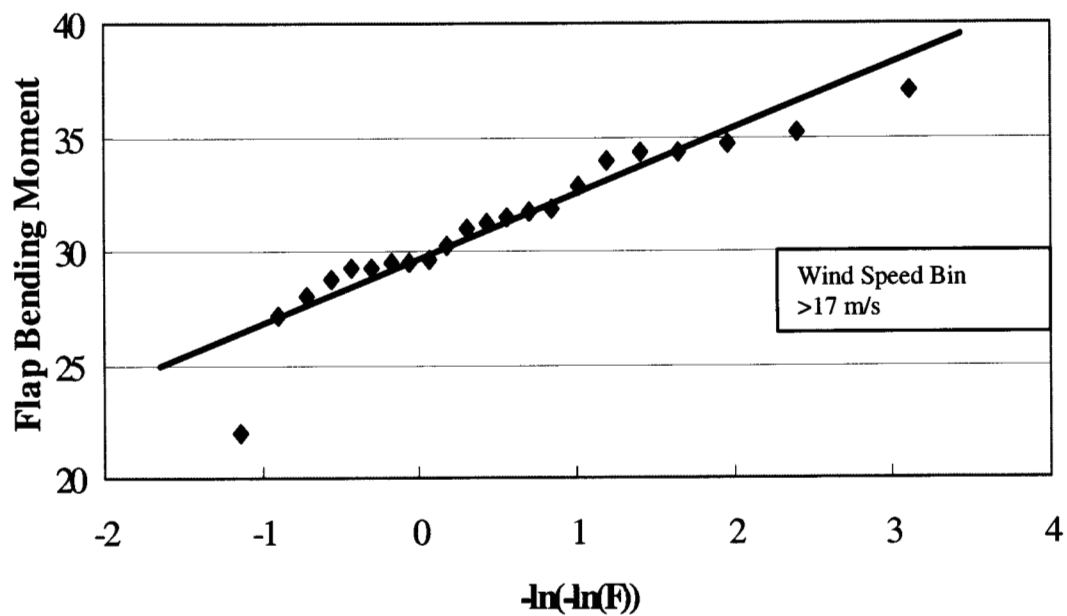


Fig. 28b. Flap-Bending Loads.

Fig. 28. Gumbel Distribution of the Load Extremes for Bin Class 8 Wind Speeds.

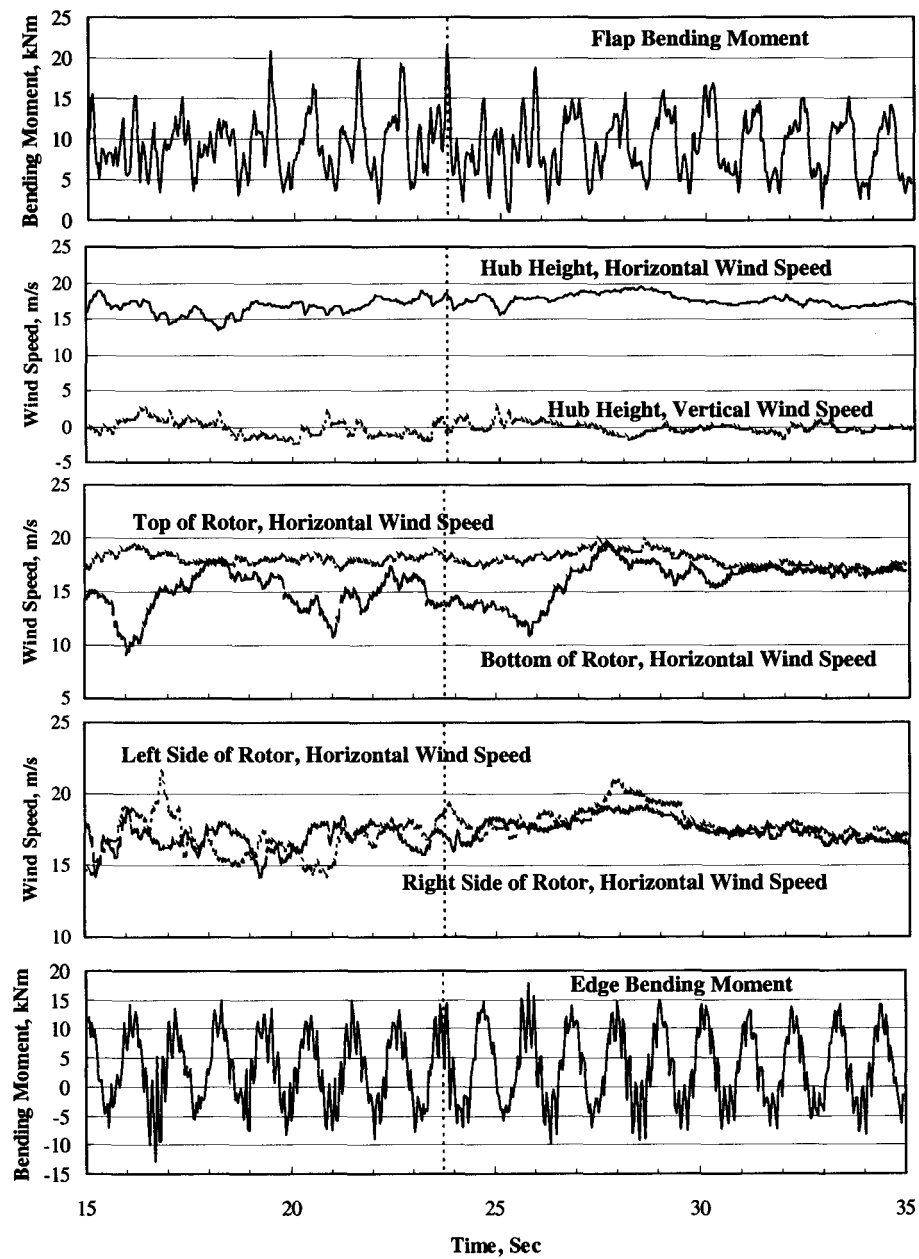


Fig. 29. Flow Field and Structural Measurements about the Extreme Flap Event for Bin Class 5 Wind Speeds.